



The 30 Year Search for the Compact Object in SN 1987A

Dennis Alp¹, Josefin Larsson¹, Claes Fransson², Remy Indebetouw³, Anders Jerkstrand⁴, Antero Ahola⁵, David Burrows⁶, Peter Challis⁷, Phil Cigan⁸, Aleksandar Cikota⁹, Robert P. Kirshner^{7,10}, Jacco Th. van Loon¹¹, Seppo Mattila⁵, C.-Y. Ng¹², Sangwook Park¹³, Jason Spyromilio⁹, Stan Woosley¹⁴, Maarten Baes¹⁵, Patrice Bouchet^{16,17}, Roger Chevalier¹⁸, Kari A. Frank¹⁹, B. M. Gaensler²⁰, Haley Gomez⁸, Hans-Thomas Janka⁴, Bruno Leibundgut⁹, Peter Lundqvist², Jon Marcaide²¹, Mikako Matsuura⁸, Jesper Sollerman², George Sonneborn²², Lister Staveley-Smith²³, Giovanna Zamarbon²³, Michael Gabler⁴, Francesco Taddia², and J. Craig Wheeler²⁴

¹Department of Physics, KTH Royal Institute of Technology, The Oskar Klein Centre, AlbaNova, SE-106 91 Stockholm, Sweden; dalp@kth.se

²Department of Astronomy, Stockholm University, The Oskar Klein Centre, AlbaNova, SE-106 91 Stockholm, Sweden

³National Radio Astronomy Observatory and University of Virginia, 520 Edgemont Road, Charlottesville, VA 22903, USA

⁴Max Planck Institute for Astrophysics, Karl-Schwarzschild-Str. 1, D-85748 Garching, Germany

⁵Tuorla observatory, Department of Physics and Astronomy, University of Turku, Väisäläntie 20, FI-21500 Piikkiö, Finland

⁶Department of Astronomy & Astrophysics, The Pennsylvania State University, University Park, PA 16802, USA

⁷Harvard-Smithsonian Center for Astrophysics, 60 Garden Street, Cambridge, MA 02138, USA

⁸School of Physics and Astrophysics, Cardiff University, Queens buildings, The Parade, Cardiff CF24 3AA, UK

⁹European Southern Observatory, Karl-Schwarzschild-Strasse 2, D-85748 Garching, Germany

¹⁰Gordon and Betty Moore Foundation, 1661 Page Mill Road, Palo Alto, CA 94304, USA

¹¹Lennard-Jones Laboratories, Keele University, ST5 5BG, UK

¹²Department of Physics, The University of Hong Kong, Pokfulam Road, Hong Kong

¹³Department of Physics, Box 19059, 108 Science Hall, University of Texas at Arlington, Arlington, TX 76019, USA

¹⁴Department of Astronomy and Astrophysics, University of California, Santa Cruz, CA 95064, USA

¹⁵Sterrenkundig Observatorium, Universiteit Gent, Krijgslaan 281 S9, B-9000 Gent, Belgium

¹⁶IRFU, CEA, Université Paris-Saclay, F-91191 Gif-sur-Yvette, France

¹⁷CNRS/AIM, Université Paris Diderot, F-91191 Gif-sur-Yvette, France

¹⁸Department of Astronomy, University of Virginia, P.O. Box 400325, Charlottesville, VA 22904-4325, USA

¹⁹Center for Interdisciplinary Exploration and Research in Astrophysics (CIERA), Northwestern University, 2145 Sheridan Road, Evanston, IL 60208, USA

²⁰Dunlap Institute for Astronomy and Astrophysics, 50 St. George Street, Toronto, ON M5S 3H4, Canada

²¹Departamento de Astronomía y Astrofísica, Universidad de Valencia, Dr. Moliner 50, Burjassot-Valencia, E-46100, Spain

²²Laboratory for Observational Cosmology, Code 665, NASA Goddard Space Flight Center, Greenbelt, MD 20771, USA

²³International Centre for Radio Astronomy Research (ICRAR), University of Western Australia, 35 Stirling Hwy, Crawley, WA 6009, Australia

²⁴Department of Astronomy and McDonald Observatory, The University of Texas at Austin, Austin, TX 78712, USA

Received 2018 May 11; revised 2018 July 27; accepted 2018 July 28; published 2018 September 13

Abstract

Despite more than 30 years of searching, the compact object in Supernova (SN) 1987A has not yet been detected. We present new limits on the compact object in SN 1987A using millimeter, near-infrared, optical, ultraviolet, and X-ray observations from ALMA, VLT, *HST*, and *Chandra*. The limits are approximately 0.1 mJy ($0.1 \times 10^{-26} \text{ erg s}^{-1} \text{ cm}^{-2} \text{ Hz}^{-1}$) at 213 GHz, $1 L_{\odot}$ ($6 \times 10^{-29} \text{ erg s}^{-1} \text{ cm}^{-2} \text{ Hz}^{-1}$) in the optical if our line of sight is free of ejecta dust, and $10^{36} \text{ erg s}^{-1}$ ($2 \times 10^{-30} \text{ erg s}^{-1} \text{ cm}^{-2} \text{ Hz}^{-1}$) in 2–10 keV X-rays. Our X-ray limits are an order of magnitude less constraining than previous limits because we use a more realistic ejecta absorption model based on three-dimensional neutrino-driven SN explosion models. The allowed bolometric luminosity of the compact object is $22 L_{\odot}$ if our line of sight is free of ejecta dust, or $138 L_{\odot}$ if dust-obscured. Depending on assumptions, these values limit the effective temperature of a neutron star (NS) to $< 4\text{--}8 \text{ MK}$ and do not exclude models, which typically are in the range 3–4 MK. For the simplest accretion model, the accretion rate for an efficiency η is limited to $< 10^{-11} \eta^{-1} M_{\odot} \text{ yr}^{-1}$, which excludes most predictions. For pulsar activity modeled by a rotating magnetic dipole in vacuum, the limit on the magnetic field strength (B) for a given spin period (P) is $B \lesssim 10^{14} P^2 \text{ G s}^{-2}$, which firmly excludes pulsars comparable to the Crab. By combining information about radiation reprocessing and geometry, we infer that the compact object is a dust-obscured thermally emitting NS, which may appear as a region of higher-temperature ejecta dust emission.

Key words: stars: black holes – stars: neutron – supernovae: individual (SN 1987A)

1. Introduction

Supernova (SN) 1987A provides a unique opportunity to observe the development of an SN and the subsequent early evolution of a very young SN remnant (for reviews of SN 1987A, see Arnett et al. 1989; McCray 1993; McCray &

Fransson 2016). SN 1987A is expected to have created a compact object. The existence of the compact object is supported by the detection of the initial neutrino burst, which was observed by Kamiokande II (Hirata et al. 1987, 1988) and the Irvine–Michigan–Brookhaven detector (Bionta et al. 1987; Bratton et al. 1988), with a possible supporting detection by the Baksan Neutrino Observatory (Alekseev et al. 1987; Alexeyev et al. 1988). While the prompt neutrino emission is attributed to the formation of a compact object, more than 30 years of diligent searches across the electromagnetic spectrum have

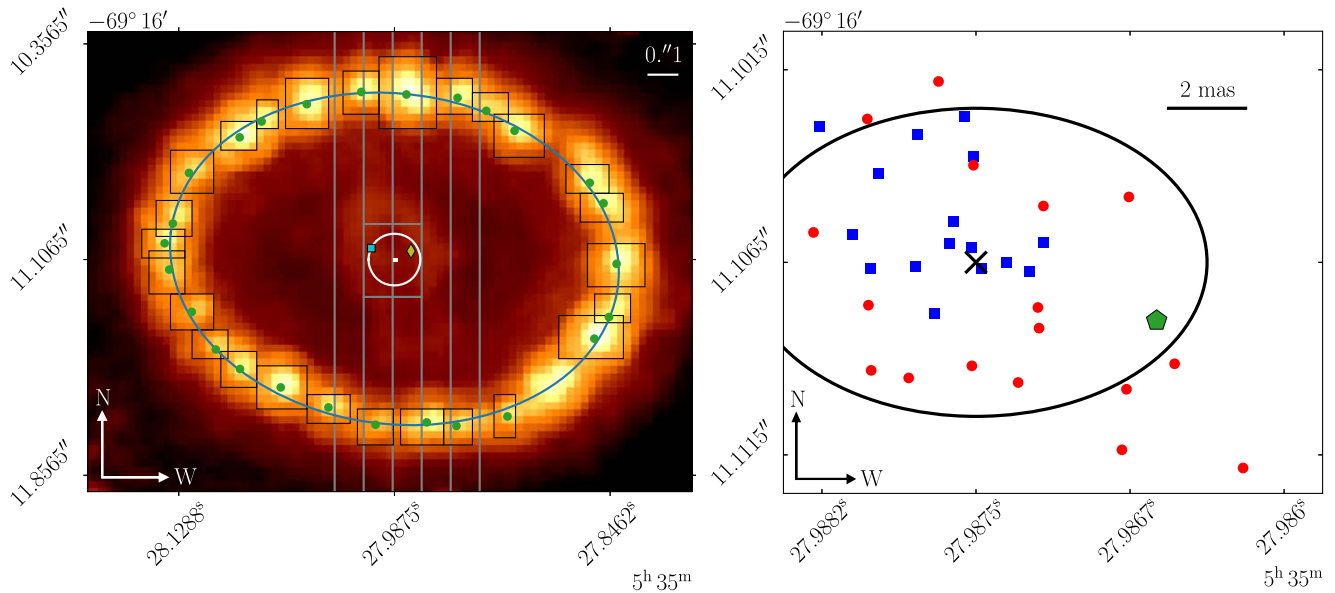


Figure 1. Position estimates of SN 1987A plotted on the *HST*/ACS F625W 2006 December 6 observation. The left panel shows the fitted hotspot locations as green dots, which are determined by fitting two-dimensional (2D) Gaussians within the black rectangles. The blue ellipse is the best-fit ellipse to the green dots and the (very small) white rectangle is the entire region shown in the right panel. The white circle is the search region corresponding to a kick velocity of 800 km s^{-1} at 10,000 days (2014 July 11). The cyan square is the radio centroid position (fit of a spherical shell to radio data) and the yellow diamond is the progenitor position reported by Reynolds et al. (1995) after correcting for the proper motion of the position of SN 1987A in the LMC (Kallivayalil et al. 2013; van der Marel & Kallivayalil 2014; van der Marel & Sahlmann 2016). The vertical gray lines show the area covered by the five slits of the *HST*/STIS observations and the horizontal gray lines represent the STIS extraction region. The right panel shows the estimated positions of SN 1987A based on the 33 *HST* observations from 2003 to 2016 by fitting ellipses to the hotspots. The size of the right panel is $14 \times 12 \text{ mas}$. The blue points denote positions from *B*-band images and the red points denote positions from *R*-band images. The black solid ellipse is the 1σ confidence contour of the best estimate (black cross): $\alpha = 05^{\text{h}} 35^{\text{m}} 27^{\text{s}}.9875(11)$, $\delta = -69^{\circ} 16' 11''.107(4)$ (ICRF J2015.0). The green pentagon is the position (5 mas from the favored position) based on fits using an elliptic annulus as described in the text.

failed to observe it. Being able to observe the compact object in SN 1987A would provide valuable insight into the explosion mechanisms of SNe, the connection between SN progenitors and compact objects, and the early evolution of neutron stars (NSs). This has implications for our description of fundamental physics in the strong-gravity regime.

Previous studies have been able to indirectly infer some properties of the compact object in SN 1987A. The progenitor star, Sanduleak $-69^{\circ} 202$ (Sanduleak 1970), was identified as a B3 Ia blue supergiant (Kirshner et al. 1987; Walborn et al. 1987; West et al. 1987; White & Malin 1987). The zero-age main-sequence mass of the progenitor is estimated to be in the range $16\text{--}22 M_{\odot}$, and the progenitor mass is estimated to be $14 M_{\odot}$ at the time of explosion (Fransson & Kozma 2002; Smartt et al. 2009; Utrobin et al. 2015; Sukhbold et al. 2016). Most studies predict that the collapse of a star like Sanduleak $-69^{\circ} 202$ would create an NS, which is supported by the prompt neutrino burst (Burrows 1988) and SN simulations (Fryer 1999; Perego et al. 2015; Ertl et al. 2016; Sukhbold et al. 2016). However, some authors have advanced the hypothesis that a black hole (BH) was created in SN 1987A (Brown et al. 1992; Blum & Kushnir 2016). The mass estimates of the possible NS are only loosely constraining. Early estimates based on the neutrino signal predict a baryonic NS mass in the range $1.2\text{--}1.7 M_{\odot}$ (Burrows 1988), explosion simulations calibrated to SN 1987A estimate a baryonic mass of $1.66 M_{\odot}$ (Perego et al. 2015), and a lower limit on the baryonic mass of $1.7 M_{\odot}$ has been placed through constraints on explosive silicon burning by measuring Ni/Fe ratios (Jerkstrand et al. 2015).

The detection of the compact object is made difficult by the light from the ejecta and surrounding circumstellar medium (CSM). The CSM is in the form of a triple-ring structure,

possibly created by a binary merger 20,000 years before explosion (Blondin & Lundqvist 1993; Morris & Podsiadlowski 2007, 2009) or a rapidly rotating progenitor (Chita et al. 2008). The brightest of the three rings is the inner equatorial ring (ER), which is seen in Figure 1. It appears elliptical because it is inclined by $\sim 43^{\circ}$ (Tziamtzis et al. 2011). The outer parts of the SN ejecta reached the ER by 1995. The interactions gave rise to the first hotspot (Lawrence et al. 2000) and the ER subsequently brightened during several years across the entire electromagnetic spectrum (Ng et al. 2013; Fransson et al. 2015; Arendt et al. 2016; Frank et al. 2016). However, the mid-infrared emission from the ER started decreasing in 2010 (MIR, Arendt et al. 2016), the optical emission started decreasing in 2009 (Fransson et al. 2015), and the soft X-ray luminosity flattened around 2013 (Frank et al. 2016). The radiation from central ejecta is also affected by the ER. Larsson et al. (2011) showed that the brightening of the SN ejecta in the optical most likely is explained by the increase of X-ray emission from the ER. However, the decay of ^{44}Ti is still expected to be the dominant energy source in the innermost parts of the ejecta, where the compact object is expected to reside (Fransson et al. 2013; Larsson et al. 2013).

In this paper, we place limits on the compact object in SN 1987A using observations from the Atacama Large Millimeter/submillimeter Array (ALMA) at millimeter wavelengths, the Very Large Telescope (VLT) in near-infrared (NIR), *Hubble Space Telescope* (*HST*) in optical and ultraviolet (UV), and *Chandra* in X-rays. We then discuss the implications of the limits on physical properties of the compact object and prospects for future observations.

This paper is organized as follows. The observations and data reduction are presented in Section 2 and the analysis methods are presented in Section 3. We present our compact

Table 1
Observations of SN 1987A

Instrument	Epoch (YYYY mm dd)	Exposure (s)	Band/Filter/Grating	Frequency/Wavelength/Energy
ALMA	2014 Sep 02	1800–2040 ^a	6	230 GHz
VLT/NACO	2010 Oct 26	2160 ^b	<i>H</i>	1.7 μm
VLT/NACO	2012 Dec 14	2070 ^c	<i>K_s</i>	2.2 μm
VLT/SINFONI	2014 Oct 10	2400 ^d	<i>H</i>	1.7 μm
VLT/SINFONI	2014 Oct 12	2400 ^d	<i>K</i>	2.2 μm
<i>HST</i> /WFC3	2009 Dec 13	800	F438W	4300 Å
<i>HST</i> /WFC3	2009 Dec 13	3000	F625W	6300 Å
<i>HST</i> /WFC3	2009 Dec 12	800	F225W	2400 Å
<i>HST</i> /WFC3	2009 Dec 13	800	F336W	3400 Å
<i>HST</i> /WFC3	2009 Dec 12	400	F555W	5300 Å
<i>HST</i> /WFC3	2009 Dec 13	400	F841W	8100 Å
<i>HST</i> /WFC3	2011 Jan 05	403	F110W	1.2 μm
<i>HST</i> /WFC3	2011 Jan 05	805	F160W	1.5 μm
<i>HST</i> /WFC3	2015 May 24	1200	F438W	4300 Å
<i>HST</i> /WFC3	2015 May 24	1200	F625W	6300 Å
<i>HST</i> /STIS	2014 Aug 16	40490 ^e	G750L	5300–10000 Å
<i>Chandra</i> /ACIS	2015 Sep 17	66598	HETG ^f	0.3–10 keV

Notes.

^a Different exposures for individual segments.

^b Integrated from single exposures of 120 s.

^c Integrated from single exposures of 90 s.

^d Integrated from single exposures of 600 s.

^e Sum of 8098 s for each of the five slits.

^f Only zeroth-order image and CCD spectrum used for the analysis.

object limits in Section 4 and discuss the implications of our results in Section 5. Finally, we summarize and list the main conclusions in Section 6. In an accompanying paper (Alp et al. 2018), we estimate the X-ray absorption in SN ejecta using three-dimensional (3D) neutrino-driven explosion models.

2. Observations and Data Reduction

All observations are summarized in Table 1. We use the most recent observations available at the time of analysis, unless previous ones have better quality. It is possible that older observations place more stringent constraints if the compact object was brighter in the past. We briefly inspect an X-ray observation from 2000 (Section 2.6), in addition to a detailed study of the 2015 X-ray observation, but investigating all observations of SN 1987A is beyond the scope of this paper. Some consequences of the temporal evolution of the compact object are discussed in Section 5.5.

We also analyze a circular polarimetric observation using the FOcal Reducer and low dispersion Spectrograph 2 (FOR2) at the VLT, which did not detect any significant polarization. The polarization observation is presented in Appendix A.

2.1. ALMA

ALMA observations of SN 1987A (Table 1) at 1.3 mm (Band 6, 211–275 GHz) were performed on two different epochs: Cycle 2 modest angular resolution data (2013.1.00280; 23–770 k λ) were obtained on 2014 September 2. The quasar J0519-4546 (05:19:49.72, $-45:46:43.85$; 0.75 Jy at 234 GHz) was the absolute flux calibrator, which is monitored regularly and calibrated against solar system objects by the observatory. The quasar J0635-7516 (06:35:46.51, $-75:16:16.82$; 0.68 Jy at 234 GHz) was the phase calibrator.

Cycle 3 high-angular-resolution data (2015.1.00631; 190–8600 k λ) were obtained from 2015 November 1 to 15 using J0601-7036 (06:01:11.25, $-70:36:08.79$; 0.70 Jy at 224 GHz; 0.58 Jy at 253 GHz) as the phase calibrator. Data from 211 to 213 GHz used J0519-4546 (0.75 Jy at 224 GHz) as the absolute flux calibrator. Data at 247 GHz used J0519-4546 for one execution, and J0334-4008 (03:34:13.65, $-40:08:25.10$; 0.44 Jy at 253 GHz) for a second execution. All of these quasar calibrators are observed regularly as part of the observatory calibration network, so we can evaluate the temporal evolution of each to estimate the uncertainty in the absolute flux calibrator due to quasar variability. We can then compare the derived flux densities of the phase calibrator to the monitoring observations to estimate the uncertainty in fluxscale transfer to the science target. These combined yield an estimated absolute flux calibration uncertainty of better than 7%.

We use the Common Astronomy Software Application²⁵ (CASA, McMullin et al. 2007) to calibrate and image the interferometric data into 3 images with spectral ranges deemed to be largely free of line emission: 211.83–213.25 GHz, 232.55–233.52 GHz, and 245.95–247.20 GHz (see Figure 2 of Matsuura et al. 2017). For imaging we use the task `tclean` with multiscalar deconvolution with scales of 0 and 7 times the 6² mas² pixel size. The FWHM of the restoring beam of the 213 GHz image is 57×40 mas² (major and minor axis), the 233 GHz image 49×30 mas², and the 247 GHz image 40×34 mas². Analysis of the phase rms during the observation with knowledge of the ALMA calibration efficacy (Asaki et al. 2014) leads us to conclude that the astrometric accuracy is better than 10 mas. After image reconstruction, the real-space

²⁵ <https://casa.nrao.edu>

images are transformed by a linear mapping such that the beams are circular for optimal performance with the finding algorithm, which is described in Appendix B.

2.2. VLT/NACO

SN 1987A has been observed for a total of six epochs between 2006 and 2017 with the Nasmyth Adaptive Optics System Near-Infrared Imager and Spectrograph (NACO) at the VLT (Lenzen et al. 2003; Rousset et al. 2003). Full details of the observations and data reductions are given in A. Ahola et al. (in preparation). For the present work we selected only a single epoch of H -band and K_s -band imaging of the highest image quality (Table 1). The H -band observation is from 2010 October, with a total on-source integration time of 2160 s. The K_s -band observation is from 2012 December, with a total on-source integration time of 2070 s.

The images are reduced using standard recipes from the ESO pipeline (Schreiber et al. 2004; Modigliani et al. 2007) and IRAF. A horizontal striping pattern present in the images is removed by a custom script that creates a one-dimensional (1D) image from the medians of the image pixels along the detector rows. This 1D image is then subtracted from the rows of the original image. A running sky subtraction is performed for sets of three stripe-removed exposures at a time using an ESO pipeline recipe. The three sky-subtracted exposures are aligned and stacked by the recipe yielding one sky-subtracted image per running set of three exposures. This process is repeated until all of the sets of three exposures have been sky-subtracted such that N exposures resulted in $N - 2$ sky-subtracted images. The sky-subtracted images are finally aligned based on the centroid coordinates of a bright star manually selected in each image and subsequently median-averaged. The stripe removal script is run once more for the stacked image to remove any remaining stripes and bands left by the first stripe removal step.

Flux calibrations of the NACO observations are made using star 2 as²⁶ a reference. We confirmed that star 2 is not variable using observations from 1997 to 2006 from the Near Infrared Camera and Multi-Object Spectrometer at the VLT in the F160W and F205W filters. The NACO H and K_s fluxes of star 2 are obtained by converting²⁷ the H and K_s fluxes from 2MASS (Cohen et al. 2003; Skrutskie et al. 2006). The accuracy of this zero-point construction is checked by repeating the 2MASS–ESO comparison for star 3.²⁸ The relative difference in the flux is a factor of 1.06 in the H band and 0.82 in the K_s band. We note that star 3 shows variability within a factor of two in the optical (Walborn et al. 1993), which is confirmed by regular *HST* observations in the R and B bands over the past two decades.

2.3. VLT/SINFONI

The SINGle Faint Object Near-IR Investigation (SINFONI) Integral Field Spectrograph at the VLT (Eisenhauer et al. 2003; Bonnet et al. 2004) observed SN 1987A in the H and K bands between 2014 October and December (Table 1). SINFONI provides moderate angular resolution and high spectral resolution in a small field of view (FOV). We only use the spatial resolution to extract spectra from a search region (Section 3.2). The limits are then constructed from the

extracted spectra. The data are reduced using the standard ESO pipeline (Schreiber et al. 2004; Modigliani et al. 2007) with the improved subtraction of the OH airglow emission following Davies (2007). A more detailed presentation of the processing of these particular observations is provided by Larsson et al. (2016) and a comprehensive description of SINFONI data reduction can be found in Kjær et al. (2010).

Contaminating light from the ER is subtracted from the spectra of the central region. The lines from the ER have an FWHM of $\sim 300 \text{ km s}^{-1}$ and the lines from the central ejecta have an FWHM of $\sim 2500 \text{ km s}^{-1}$ (Fransson et al. 2015; Larsson et al. 2016). Even though the ejecta are clumpy and illumination is non-uniform, the line profiles of the ejecta are relatively smooth and much broader than the sharp narrow lines from the ER. The difference allows us to subtract the ER spectra from the central spectra by scaling the ER spectra such that they cancel the narrow components of the central spectra. Backgrounds are constructed from the cleanest available regions in the relatively small FOV of SINFONI. These are then subtracted from the extracted central spectra. It is verified that different choices of background regions do not significantly alter the results. The signal-to-background ratio (S/B) for the low continuum level is 0.88 in the H band and 2.31 in the K band.

2.4. HST/WFC3

SN 1987A was observed using Wide Field Camera 3 (WFC3) in 2009 December in six filters; F225W, F336W, F438W, F555W, F625W, and F814W (Table 1). We choose these observations from 2009 because they provide the most complete wavelength coverage at a recent epoch. Together, the six filters provide coverage over the 2150–8860 Å wavelength interval. The latest WFC3 NIR observations are from 2011 January in the F110W and F160W filters. The latest wide-filter observations with high quality at the time of analysis are from 2015 May in the F438W and F625W filters.

All observations were performed using the four-point box dither pattern and drizzled (Fruchter & Hook 2002) onto a final pixel size of 25^2 mas^2 using a value for the DrizzlePac (Gonzaga et al. 2012) parameter `pixfrac` of either 0.6 or 0.7. Cosmic-ray rejection is also performed when drizzling to combine the dithered exposures. The flux zero-points for all WFC3 images are taken from the IRAF/STSDAS package Synphot (Bushouse & Simon 1994, calibration database updated on 2017 January 17).

2.5. HST/STIS

Between 2014 August 16–20, the *HST*/Space Telescope Imaging Spectrograph (STIS) observed SN 1987A using the G750L grating, which covers the wavelength interval 5300–10000 Å (Table 1). The STIS observations were described in detail in Larsson et al. (2016). Here, we provide additional information on astrometry and background subtraction because of their importance to the compact object limit. The observations were made at five adjacent slit positions, as shown in Figure 1. Each slit is 100 mas wide and oriented in the north–south direction. The position of SN 1987A that is presented in Section 3.1 is very close to the dividing line between the second and third slits.

Contaminating light from the ring is subtracted from the spectrum of the central region using the same method used

²⁶ 2MASS J05352761-6916089.

²⁷ http://www.ipac.caltech.edu/2mass/releases/allsky/doc/sec6_4b.html

²⁸ 2MASS J05352822-6916118.

for SINFONI (Section 2.3). In addition, a background is extracted from regions north and south of the SN and subtracted from the ejecta spectrum. The S/B is 0.74 for the low continuum level. The background is extracted from 75 pixel rows ($50 \text{ mas pixel}^{-1}$) in three regions both north and south of the SN 1987A.

2.6. Chandra

Chandra observed SN 1987A on 2015 September 17 (Obs.ID 16756, Table 1), utilizing the Advanced CCD Imaging Spectrometer (ACIS, Garmire et al. 2003) S-array equipped with the High-Energy Transmission Grating (HETG, Canizares et al. 2005). The ACIS detector provides imaging capabilities with an angular resolution of 700 mas (FWHM) and a moderate energy resolution of $\sim 100 \text{ eV}$ at 2 keV. The spatial resolution is just enough to resolve SN 1987A, which allows us to extract a spectrum of the central region that can be used to set an upper limit on the compact object. Among many *Chandra* observations (e.g., Frank et al. 2016), we choose this particular observation because it was the latest observation at the time of analysis, which implies that the absorption toward the center is the lowest (Appendix C).

Contamination on the ACIS optical blocking filter (OBF, O’Dell et al. 2013) has previously led to inaccurate flux measurements (e.g., Park et al. 2011; Helder et al. 2013). Frank et al. (2016) have verified that the OBF contamination is now well-modeled using the High Resolution Camera/Low Energy Transmission Grating observation of SN 1987A from 2015 March 14 (Obs.ID 16757), which does not suffer from the OBF contamination. Only data from the zeroth-order image in energy range 0.3–10 keV of the 2015 September 17 ACIS/HETG observation are used in this analysis.

The data are reduced following standard procedures using CIAO 4.9 and CALDB 4.7.7 (Fruscione et al. 2006). No background flares are observed resulting in a total exposure of 66 ks with $\sim 11,000$ source counts. XSPEC 12.9.1p (Arnaud 1996) is used for the spectral analysis and all extracted spectra are binned with a minimum of 20 counts per bin. A background is extracted from an annulus with an inner radius of $15''$ and outer radius of $30''$. The background is negligible for the spectra of SN 1987A because of the high source count rates and small spatial region of interest.

The HETG provides dispersed spectra and also reduces pileup in the zeroth-order image (Helder et al. 2013; Frank et al. 2016). The dispersed spectra are used to verify that pileup is not significant in the zeroth-order CCD spectrum and we find that bad grades 1, 5, and 7 combine to be $\sim 3\%$ of the total level 1 source counts.²⁹ This indicates that the level of pileup is low enough to not significantly affect our analysis. A more detailed treatment of pileup is difficult because SN 1987A is marginally resolved and we primarily use the spectrum from the region inside the ER, which is smaller than a single ACIS pixel. Pileup properties could be different for the ER and the ejecta because the count rate is significantly higher in the pixels neighboring the few central pixels. However, the grades are assigned based on 3×3 pixel islands. The way in which these effects combine requires custom methods, which would be excessive for our analysis.

3. Methods

Below, we describe the methods used to determine upper limits on the compact object in SN 1987A. The position of SN 1987A and the spatial regions in which we search for the compact object are described in Sections 3.1 and 3.2. Sections 3.3–3.5 present how the image and spectral limits at millimeter, UV, optical, and NIR (UVOIR) wavelengths are determined. The spread light in the X-ray observation, which complicates the computation of the X-ray limits, is described in Section 3.6. Finally, the X-ray ejecta absorption model based on 3D neutrino-driven SN explosion models (Alp et al. 2018) is described in Appendix C, and the spatial alignment of the images is described in Appendix D.

The source luminosity limits based on the imaging analysis rely on the assumption that the compact object is a point source. The limits from the spectral analysis in UVOIR are based on the assumption that the compact object emission is a continuum. Finally, the X-ray limits are constructed by assuming certain spectra for the compact object. The distance to SN 1987A is taken to be 51.2 kpc (Panagia et al. 1991; Gould & Uza 1998; Panagia 1999; Mitchell et al. 2002). All two-sided confidence intervals are 1σ and all one-sided upper limits are 3σ unless otherwise stated.

3.1. Position of SN 1987A

We need an accurate position estimate of SN 1987A because we only search for the compact object in a kick region that has a radius of $\sim 100 \text{ mas}$ (Section 3.2). Therefore, it is important that the position estimate of SN 1987A is accurate to $\sim 10 \text{ mas}$. The “position of SN 1987A” refers to the projected position of the progenitor star at current epochs. The position is determined by fitting an ellipse to the hotspots in the ER in *HST* images. This assumes that the progenitor is located at the center of the ring of hotspots. The first step is to tie the *HST* images to *Gaia* data release 1 (DR1, Gaia Collaboration et al. 2016b, 2016a) because the error of the absolute astrometry of *HST* is relatively large. This is done by mapping two unsaturated stars.³⁰ The uncertainties in the positions of the two reference stars in the *Gaia* archive are $< 1 \text{ mas}$ and the accuracies of the localizations of the stars in the *HST* images are a few mas.

All 33 observations from 2003 to 2016 in the *B* (F435W, F438W, and F439W) and *R* (F625W and F675W) bands (presented in Appendix E) are used for determining the position. Observations from before 2003 are excluded because the low number of hotspots present before this time make the fits inaccurate. The hotspots are defined using the F625W 2006 December 6 observation because it provides the best spatial resolution at an epoch when most hotspots were bright (Fransson et al. 2015). Two-dimensional (2D) Gaussians are fitted to the 26 hotspots, shown in Figure 1. The hotspots are located in the other observations by fitting a radial, one-dimensional (1D) Gaussian along the angles defined by the 2D fits in the F625W 2006 December 6 observation. This ensures that the same hotspots are found in all observations. Ellipses are then fitted to the hotspots in all images. The best-fit estimates of the position of SN 1987A from the 33 images agree within 25 mas and are shown in Figure 1 (right). The arithmetic mean of the 33 best-fit coordinates are

²⁹ <http://cxc.harvard.edu/proposer/POG/html/chap6.html>

³⁰ *Gaia* source ID: 4657668007091797248, 4657668075811272704.

$\alpha = 05^{\text{h}} 35^{\text{m}} 27^{\text{s}}.9875(11)$, $\delta = -69^{\circ} 16' 11''.107(4)$ (ICRF J2015.0), where the 1σ uncertainties are estimated by bootstrapping the hotspot locations. Unless otherwise stated, all presented coordinates are at epoch J2015.0 and in the reference frame of *Gaia* DR1, which is effectively equivalent to ICRF (the realization of ICRS) for the current level of precision. This will henceforth be adopted as the position of SN 1987A in this work.

We emphasize that the reported confidence interval only represents the statistical uncertainty. Fitting to the ER continuum in the ALMA observation results in a position offset of approximately 60 mas to the east, but the ER is more diffuse at millimeter wavelengths and we choose to use the optical observations. This is likely to be the best approach because the hotspots are well-defined point sources, whereas the millimeter emission originates from a larger volume above and below the optically emitting ring.

The systematic error introduced by assuming the hotspots to be located in an ellipse centered on the supernova position is checked by fitting an elliptic annulus with a Gaussian radial profile to the entire inner ring. This elliptical band is also allowed to rotate in the sky plane and has a sinusoidal intensity along the azimuth. This describes the inner ring as a continuum rather than as a collection of point sources and serves as a relatively independent estimate of the position. The center obtained using an elliptical annulus is $\alpha = 05^{\text{h}} 35^{\text{m}} 27^{\text{s}}.9866$, $\delta = -69^{\circ} 16' 11''.108$ (ICRF J2015.0), as shown in Figure 1 (right, green pentagon). This position is offset by 5 mas from the favored position of SN 1987A.

The hotspot coordinates can be compared to the best estimate of the location of the progenitor star Sanduleak $-69^{\circ} 202$; $\alpha = 05^{\text{h}} 35^{\text{m}} 27^{\text{s}}.968(9)$, $\delta = -69^{\circ} 16' 11''.09(5)$ (ICRF J1991.5, Reynolds et al. 1995). In addition, Reynolds et al. (1995) used observations by the Australia Telescope Compact Array from 1992 October 21 and 1993 January 4–5 at 8.8 GHz and reported a radio centroid position; $\alpha = 05^{\text{h}} 35^{\text{m}} 27^{\text{s}}.994(12)$, $\delta = -69^{\circ} 16' 11''.08(5)$ (ICRF J1991.9). The aforementioned coordinates are those reported by Reynolds et al. (1995). To compare with our estimates in Figure 1, the positions of Reynolds et al. (1995) are corrected for the displacement between the epochs of observation. The proper motion of the position of SN 1987A in the Large Magellanic Cloud (LMC) is 46 mas east and 13 mas north (Kallivayalil et al. 2013; van der Marel & Kallivayalil 2014; van der Marel & Sahlmann 2016). This assumes that the proper motion of Sanduleak $-69^{\circ} 202$, and consequently also SN 1987A, conforms to the expected motion of its location within the LMC.

3.2. Search Region

An extended region is searched because the compact object created by SN 1987A is expected to have a kick velocity caused by the asymmetric explosion. Typical 3D kick velocities of pulsars are $\sim 400 \text{ km s}^{-1}$ (Hobbs et al. 2005; Faucher-Giguère & Kaspi 2006). However, extreme cases of velocities up to 1600 km s^{-1} have been observed (Cordes et al. 1993; Chatterjee & Cordes 2002, 2004; Hobbs et al. 2005). When searching for a point source in SN 1987A, we assume a sky-plane projected kick velocity of 800 km s^{-1} , which corresponds to a search radius of ~ 100 mas at the epoch of our observations. This is a trade-off between having to search an excessively large region and the risk of not including the true source position.

The effects of different choices of kick velocity are relatively small. For a kick of 1600 km s^{-1} , the average correction factor to the six *HST* limits from 2009 (Section 4.2) is 1.07. For a more typical speed of 400 km s^{-1} the corresponding factor is 0.86. The reason for the small difference is that the brightness is relatively uniform and the search algorithm is dependent on both surrounding morphology and brightness. This means that limits are not directly proportional to the local brightness.

3.3. Reddening

The effect of interstellar reddening at UVOIR wavelengths is corrected for using the model of Cardelli et al. (1989) with $R_V = 3.1$ and $E(B - V) = 0.19$. The parameters are chosen based on the work by France et al. (2011), which takes several studies of extinction to SN 1987A and the LMC into consideration (Fitzpatrick & Walborn 1990; Walker & Suntzeff 1990; Scuderi et al. 1996; Gordon et al. 2003; Michael et al. 2003). The uncertainty in the de-reddening is approximately 20% below 3000 \AA , less than 10% in the optical, and less than $\sim 2\%$ in the NIR.

Large amounts of dust have been detected in the ejecta of SN 1987A (Matsuura et al. 2011, 2015; Indebetouw et al. 2014; Dwek & Arendt 2015; Wesson et al. 2015), but we do not attempt to correct for it using the same method used for interstellar reddening. The primary reason for this is that the spatial distribution of the ejecta dust is poorly constrained (e.g., Dwek & Arendt 2015; Wesson et al. 2015). Our treatment of ejecta dust is explained in Section 4.1.

3.4. Image Limits

Image limits are obtained from ALMA, VLT/NACO, and *HST*/WFC3. The same method is used for all observations, apart from two small differences for ALMA. The differences are how the PSFs of the instruments are determined and how the spatial positions are chosen. For the interferometric ALMA images, the PSFs are the well-defined reconstruction beams (Section 2.1). The PSFs for the UVOIR images are created using the IRAF/DAOPHOT (Stetson 1987) package following the guidelines for fitting PSFs in Davis (1994). An empirical PSF is generated for each observation by fitting to ~ 10 bright, well-isolated stars. A Gaussian is selected as the analytical component with a linear lookup table. The quality of the PSFs is checked by estimating the residuals when subtracting best fits from the original images. The residuals are less than 5% of the counts for most stars. In addition, each individual PSF model is visually inspected for defects.

The ALMA limits are not required to be from the same point because they are treated as three independent limits in the analysis. In contrast, UVOIR image limits from the same epoch are at the same spatial position for the different bands. The points are chosen such that the highest total flux allowed by the limits in all bands is maximized and allows us to combine the limits to constrain spectra.

The remainder of the process is identical for the ALMA and UVOIR images. Limits are obtained by introducing artificial sources with known fluxes that are recovered using a finding algorithm, which is described in Appendix B.

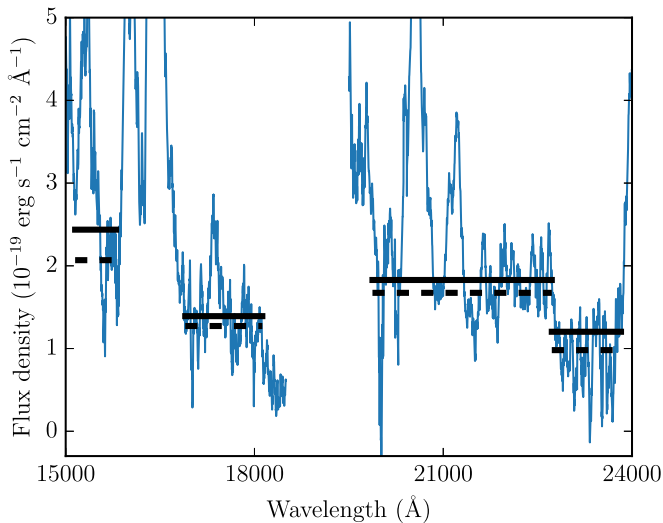


Figure 2. The 2014 SINFONI *H* and *K* spectra of the central region of SN 1987A. Both spectra are extracted from regions that correspond to the 800 km s^{-1} kick region (Section 3.2, Figure 1). The solid black lines are the upper limits and the dashed black lines are the average flux in the selected intervals (Section 3.5.1). The spectra have been corrected for spread light from the ER and background-subtracted (Section 2.3), and corrected for interstellar reddening (Section 3.3). The observed spectra (blue) have been binned by a factor of 21 for visual clarity.

3.5. Spectral Limits

The spectra are extracted from regions corresponding to the 800 km s^{-1} kick region and wavelengths are corrected for the systematic heliocentric velocity of SN 1987A of 287 km s^{-1} away from Earth (Gröningson et al. 2008a, 2008b). Limits are then constructed from spectral regions that are relatively free of line emission. These regions are assumed to contain contributions from weak lines, gas continuum emission, and emission from the compact object. Therefore, the determined limits are conservative limits on the contribution from the compact object. We fit functions to the observed flux within the regions that are free of line emission (Sections 3.5.1 and 3.5.2). The magnitudes of these functions are then increased until the χ^2 values have increased by 7.740. These values are then taken to be the one-sided 3σ upper limits. We verified that the reduced χ^2 values are reasonably close to unity, which is required for this method to be applicable.

3.5.1. NIR Spectral Limits

The upper limits from the SINFONI spectra are set using the flux density in regions that are free of strong line emission. The resulting spectra are shown in Figure 2. The regions are selected to avoid intervals of emission lines identified in SN 1987A provided in Tables 3 and 4 of Kjær et al. (2007) and regions of H_2 emission (Fransson et al. 2016). Moreover, wavelength intervals close to residual atmospheric lines are also excluded. These are clearly seen in observations as narrow lines. In total, 16% of all data pass the aforementioned selection criteria in the *H* band; for the *K* band, 28% pass the criteria. We combine many very narrow intervals into four groups and define constant functions within the groups (Figure 2). We choose four regions because the specific flux is relatively constant within the regions. The constant values are the averages within each group, which are then increased to a 3σ upper-limit level.

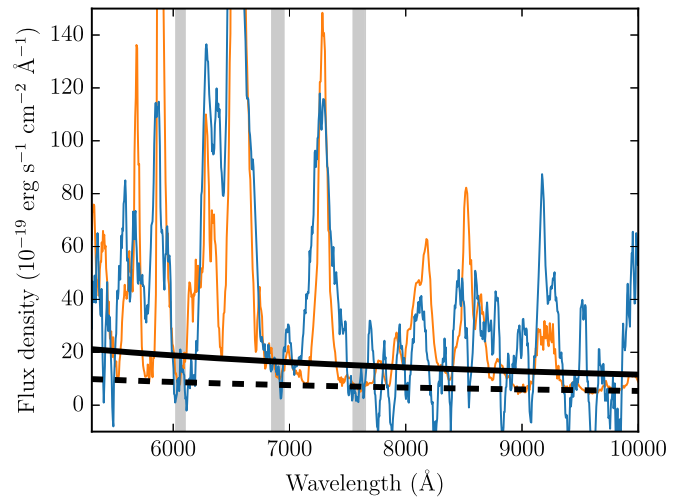


Figure 3. The 2014 STIS spectrum of the central region of SN 1987A. The extraction region is a rectangle that approximately contains the 800 km s^{-1} kick region (Section 3.2, Figure 1). The solid black line is the power law that represents the 3σ upper limit to continuum emission from a compact object. The dashed black line is the best-fit power law, which is a factor of 2.1 lower than the limit. The gray regions indicate the wavelength intervals in which the power law is fitted. The spectra have been corrected for spread light from the ER and background-subtracted (Section 2.5), and corrected for interstellar reddening (Section 3.3). The observed spectrum (blue) is smoothed by a factor of 11 for visual clarity. The orange line is a model spectrum of SN 1987A taken from Jerkstrand et al. (2011) normalized to $\text{H}\alpha$. This model is only used for identifying regions that are free of line emission.

3.5.2. Optical Spectral Limit

To determine the compact object limit using the STIS observation, a spectrum is extracted from the search region. Because of the resolution of the instrument, the spectrum is from a region with a width of two 100 mas slits and height of five 50 mas pixels, which is approximately equivalent to a rectangle that just contains the 800 km s^{-1} extraction region (Figure 1). A power law is fitted to regions that are free of strong lines (gray regions in Figure 3). The power law describes the quasicontinuum well within the STIS wavelength range 5300–10000 Å, which is why we do not use the same method as for SINFONI (Section 3.5.1). No significant improvement in the fit is seen for other simple functional forms. The selected regions that are relatively free from line emission are 6025–6100, 6850–6950, and 7550–7650 Å. The average flux in the middle region is slightly higher, but excluding it results in a $\sim 10\%$ less constraining limit because of the reduced statistics. The regions are found by visual inspection of the observed spectrum and by searching the model spectrum of Jerkstrand et al. (2011) for regions free of strong lines. The model computes an observed spectrum by simulating the radiation transfer through the SN ejecta, which is assumed to be powered by the radioactive decay of ^{44}Ti . We note that the predicted spectrum was summed over the entire ejecta and worse agreement is expected for the smaller search region. The model is only used to identify line-free regions and it is included in Figure 3 for reference.

3.6. X-Ray Limits

To determine the X-ray flux limit on the compact object, the ER emission needs to be modeled. This is important because the observed flux in the inner region is dominated by spread light from the ER. We use spread light to refer to the result of

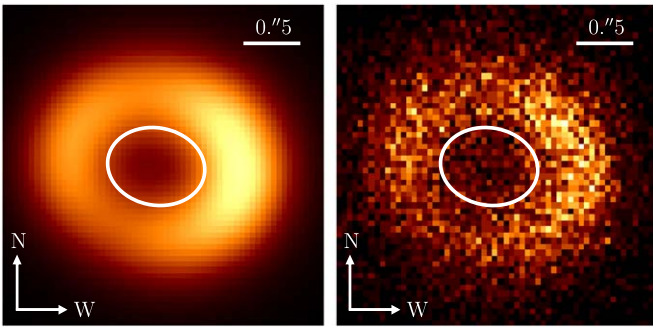


Figure 4. Folded model (left panel; see the text) and the 2015 September 17 *Chandra*/ACIS observation binned to 50^2 mas² pixels in the energy range 0.3–10 keV (right). The ellipse shows the inner region where the ejecta spectrum is extracted.

angular blurring of telescopes, also referred to as wings, leaked light, scattered light, or glare. The spatial model allows for computation of the amount of spread light in the inner region. Finally, the limits are set by spectral fitting to the spectrum from the inner region with a model that includes the spread light from the ER.

We also briefly inspected the 61 ks ACIS observation from 2000 December 7 (Obs. ID 1967) and find that the X-ray limits allow for approximately a factor of two higher luminosities because of the higher ejecta absorption (Appendix C). It is unlikely that more stringent limits can be placed using the High Resolution Camera on board *Chandra* because of the very poor energy resolution, which prevents separation of emission from the ER.

3.6.1. Spatial Modeling

The remnant is fitted with an ellipse of sinusoidal intensity along the azimuth and Gaussian radial profiles, and is then folded through the modeled instrumental PSF. This is just a model used to describe the observed morphology of the ER. A description of the simulation of the *Chandra* PSF is provided in Appendix F. The inner region covering the central ejecta is excluded from the fit to reduce the effects of any contribution from a central source. Observations show finer structure than allowed by this simple model. Therefore, the pixels of the unfolded model are given some freedom by assigning new values that are distributed as normal distributions, with the mean set to the original value and standard deviation set to one-third of the original value. Any negative values are set to zero. The random reassignment of pixels is performed 10,000 times and the folded model that gives the maximum likelihood for the observed data is chosen, as shown in Figure 4. The goodness of fit is determined by simulating 100,000 observations from the folded best-fit model. A total of 53,039 simulations resulted in a higher statistical likelihood than the real observation, showing that the fit is acceptable.

An inner and an outer region are defined using the best-fit model. These are the regions from which spectra are extracted. The inner region (Figure 4) is defined as an inclined ellipse with parameters given by the fitted model: a position angle of 83° to the semimajor axis (defined counter-clockwise from north) and a ratio of semimajor to semiminor axis of 1.37. The magnitude of the semimajor axis of the inner region is set to 450 mas, which is chosen to maximize the signal-to-noise ratio (S/N) of a central point source. This can be compared to the 870 mas semimajor axis and 620 mas semiminor axis of the

best-fit ellipse. The outer region is defined as an inclined elliptical annulus with the inner region as the inner boundary. The semimajor axis of the outer boundary of the outer region is $10''$.

An ER spectrum is extracted from the outer region and a central spectrum from the inner region, henceforth referred to as the ejecta spectrum. The ejecta spectrum has a total photon count of 624. The option to correct for the encircled energy (EE) of the CIAO task `specextract` is disabled. Instead, the correction factor for the inner region is computed to be 0.46 using the simulated MARX PSF. The value of 0.46 is computed for a point source at the center and will be used to correct for the missing flux throughout this analysis. No EE correction is applied to the outer region because the physical flux of the ER is not of interest. This method is employed because it allows for fitting of the fraction of spread light, which can then be directly compared to the modeled fraction of spread light.

3.6.2. Modeled Spread Light Fraction

Light from the bright ER contaminates the central region of SN 1987A in the *Chandra* observations. We estimate the fraction of spread light (f_s) using the spatial model and compare it to the observed value, which is obtained by spectral fitting. The fraction of spread light is defined as the ratio of spread light flux in the inner region to the flux in the outer region. The value $f_s = 0.073_{-0.005}^{+0.011}$ is computed using the spatial model with no central source. The model is forward-folded using the PSF to simulate the angular response of the detector and the uncertainties are obtained by simulations using the fitted model. We assume that the energy dependence of the EE is relatively weak, implying that the spectrum of the spread light in the inner region is the same as the spectrum of the ER itself. This assumption is partially motivated by the fact that the energy dependence is modest over the range covered by the bulk of the photons. Additionally, the small angular separations of $\lesssim 1''$ further reduce the magnitude of this effect; see Section 3.2 of Park et al. (2010) for a more detailed treatment of spread light.

3.6.3. Observed Spread Light Fraction

The observed fraction of spread light can be determined by extracting spectra from both the ER and the inner region, and then fitting the model that describes the ER to the inner spectrum, with only the normalization left free to vary. This needs to be done because there might be a significant contribution from the compact object in the observation, which is assumed to have a spectrum different from that of the ER.

The model we use for the ER spectrum consists of an ISM absorption component and three source components; an ionization equilibrium collisional plasma (`vequill`) at a temperature of 0.3 keV, a constant-temperature plane-parallel shock plasma model (`vpshock`) at a temperature of 2.1 keV, and a power-law component. ISM absorption of all three components is modeled using the `tbgrain` (Wilms et al. 2000) photoabsorption model with a frozen hydrogen column density of $N_{\text{ISM}} = 0.409 \times 10^{22} \text{ cm}^{-2}$, of which $0.144 \times 10^{22} \text{ cm}^{-2}$ is molecular. These values are taken from Willingale et al. (2013)³¹ and are approximately a factor of two higher than the value used

³¹ <http://www.swift.ac.uk/analysis/nht/>

by many previous X-ray studies of SN 1987A, which neglected the molecular component. We note that this only makes a difference of $\sim 3\%$ for our results because of the high ejecta absorption. For this reason, we also ignore any CSM or LMC absorption. The power law reduced the fit statistic by $\Delta\chi^2 = -29$ for 2 additional degrees of freedom (d.o.f.) and clearly improved the fit at energies above 5 keV. The power law does not have a clear physical interpretation, but the purpose of the model is only to represent the spread light from the ER into the central region. The fit statistic for the ER spectrum is $\chi^2 = 205$ for 202 d.o.f.

We then fit the ER model to the ejecta spectrum, with all parameters frozen apart from a constant factor. This represents an upper limit on the spread light from the ER into the central region because it is implicitly assumed that the contribution from the compact object is negligible. The fit statistic is $\chi^2 = 29.8$ for 27 d.o.f. and the fraction of spread light to ER flux is 0.062 ± 0.003 , which can be compared to the value of $0.073^{+0.011}_{-0.005}$ predicted by the model. The goodness of fit implies that the energy dependence of the EE is small enough to be neglected in this case. The observed value is marginally lower than predicted and implies that practically all flux observed in the central region can be interpreted as spread light from the ER. The purpose of comparing the modeled and observed f_s is that an observed value that is significantly higher than predicted would indicate an additional contribution in the central region.

3.6.4. Calculating X-Ray Limits

We construct X-ray limits on the compact object by adding components to the ER spectrum model and re-fitting the model to the ejecta spectrum. Then, we find the limiting value for a parameter of interest of the additional component while fitting f_s and freezing all other parameters. Leaving additional parameters free is not possible because the low number of counts in the ejecta region is insufficient to meaningfully constrain additional parameters. The additional component represents the contribution from the compact object and the SN ejecta absorption (Appendix C) is only applied to this component using the `tbvarabs` (Wilms et al. 2000) photo-absorption model. The presented results are obtained using the Levenberg–Marquardt fitting algorithm and the χ^2 statistic. We also attempted an unbinned analysis using the Cash-statistic (Cash 1979), but found differences that are much smaller than other uncertainties.

Blackbody and power-law models with different amounts of ejecta absorption are tested, as described in Section 4.4. The value f_s remained ≥ 0.06 for all models with absorption (Section 4.4), which means that the spread light is not degenerate with the additional component. The upper limits are obtained by requiring an increase of the χ^2 statistic of 7.740. This corresponds to a one-sided 3σ limit, analogous to the SINFONI and STIS spectral limits (Section 3.5).

4. Results

We describe our model of the ejecta dust absorption in Section 4.1, which is relevant for the results from the UVOIR observations, but not the other wavelengths. The direct millimeter, UVOIR, and X-ray limits are then presented in Sections 4.2–4.4. In Section 4.5, we present the bolometric limits, which are partly dependent on the UVOIR observations.

Therefore, we provide bolometric limits for both dust-free and dust-obscured lines of sight.

4.1. UVOIR Dust Absorption

The effects of absorption by ejecta dust are important in UVOIR. The dust is assumed to have a negligible impact on the millimeter observations and have the same absorption properties as gas in the X-ray regime (Morrison & McCammon 1983; Draine 2003; Alp et al. 2018). Large amounts of dust have been observed in SN 1987A (Lakićević et al. 2011, 2012a; Matsuura et al. 2011, 2015; Indebetouw et al. 2014; Dwek & Arendt 2015; Wesson et al. 2015; Bevan 2018) and there is evidence that the dust resides in clumpy structures (Lucy et al. 1989, 1991; Fassia et al. 2002; Jerkstrand et al. 2011). The latter means that the dust is modeled as a covering factor and not an average optical depth. The diameters of the clumps of molecules have been observed to be ~ 100 mas (1000 km s^{-1} or 8×10^{16} cm, Abellán et al. 2017), but it is possible that the size of the dust clumps is different from the clumps of molecules. The covering factor has been estimated to be 50%–70% by observing asymmetries of emission lines and spectral modeling (Lucy et al. 1989, 1991; Wooden et al. 1993; Wang et al. 1996; Fassia et al. 2002; Jerkstrand et al. 2011).

The information about the ejecta dust in SN 1987A is insufficient for detailed corrections. In particular, the 3D SN explosion models used for the X-ray absorption estimate (Appendix C) cannot be used for the dust because dust formation, composition, and geometry depend on additional unconstrained parameters (e.g., Bevan 2018). Instead, we assume that our line of sight to the compact object in SN 1987A is free of ejecta dust clumps when placing limits in UVOIR. If there is a dust clump along our line of sight to a compact object, then essentially all UVOIR emission from the compact object would be absorbed and the presented direct UVOIR limits would not apply.

However, we consider the reprocessing of the absorbed UVOIR emission in the dust-obscured case in Section 4.5, where we obtain bolometric limits based on the energy budget of the ejecta. We assume that the dust is optically thick throughout the UVOIR part of the spectrum because no indications of energy- or time-dependent attenuation have been observed with VLT/SINFONI (since 2005) or *HST* (since 1994, Larsson et al. 2013, 2016).

4.2. Millimeter and UVOIR Image Limits

We compute upper limits on the compact object in SN 1987A at millimeter wavelengths using the ALMA images. An image of the observation at 213 GHz is shown in Figure 5 and the limits are provided in Table 2. The ER and central ejecta structure are clearly resolved and no obvious point source is seen in any of the ALMA images. The level of spatially extended emission in the central region is comparable to the noise level. The high noise level is a consequence of constructing images of narrow frequency spans of 1–2 GHz (Section 2.1).

The upper limits in UVOIR are shown in Figure 6 and listed in Table 3. There are limits in six filters from 2009; F225W, F336W, F438W, F555W, F625W, and F841W. The more constraining limits in the *B* and *R* bands are the 2015 observations. The four NIR limits are: WFC3 F110W and F160W from 2011, and NACO *H* from 2010 and *K_s* from 2012.

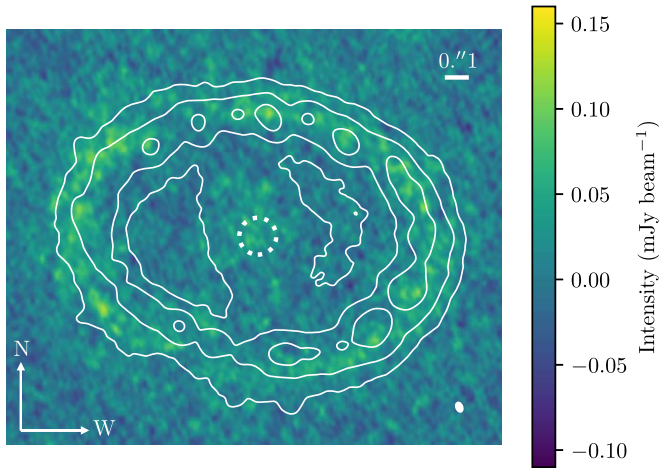


Figure 5. ALMA observation at 213 GHz (color map) and the *HST*/WFC3 observation from 2014 June 15 in the *B* band (contours). The dotted white circle is the search region (Section 3.2) and the $57 \times 40 \text{ mas}^2$ beam is shown in the lower right corner. The pixel size is 6^2 mas^2 and the off-source rms noise is $\sim 0.02 \text{ mJy beam}^{-1}$.

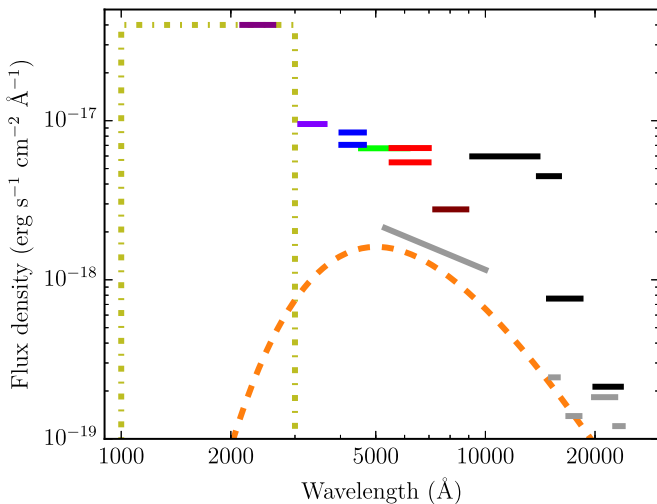


Figure 6. Limits in UVOIR on a point source in SN 1987A inside a kick region corresponding to 800 km s^{-1} . The gray lines are spectral limits. Image limits from left to right are as follows: F225W, F336W, F438W, F555W, F625W, F814W, F110W, F160W, NACO *H*, and NACO *K_s*. The less strict limits in F438W and F625W are from 2009 and are simultaneous with the other optical image limits, whereas the stricter F438W and F625W limits are from 2015. Limits from the same epoch are from the same spatial position. The dashed orange line is a blackbody spectrum for the temperature and radius of the Sun scaled to the distance of SN 1987A. This can be taken as a limit on a surviving main-sequence companion if our line of sight is free of dust (Section 5.6). The dashed-dotted yellow line is the assumed conservative spectrum corresponding to a luminosity of $6.6 L_{\odot}$ used for the bolometric limit (Section 4.5).

Table 2
Millimeter Limits

Frequency (GHz)	Flux Density (mJy)
213	0.11
233	0.20
247	0.12

All limits from the same epoch are at the same spatial position. In contrast to the ALMA images, the limits at UVOIR are dominated by the ejecta emission.

4.3. UVOIR Spectral Limits

The SINFONI *H* and *K* spectra from the central region and limits on the compact object are shown in Figures 2 and 6. The limits for the individual wavelength intervals are listed in Table 3. We note that the four intervals are for presentation only and are groups consisting of many narrow ranges, which are used to compute the limits (Section 3.5.1). Images of the selected wavelength intervals that are relatively free of line emission are also studied and no clear point source is seen in the resolved image of the ejecta. The spatial distribution of the emission in the central regions of the ejecta in the continuum images is essentially uniform at the resolution of SINFONI in both the *H* and *K* bands.

The STIS spectrum for the central region of SN 1987A is shown in Figure 3. The limiting power law is given by

$$F_{\lambda} = 1.2 \times 10^{-18} \left(\frac{\lambda}{10^4 \text{ \AA}} \right)^{-0.95} \text{ erg s}^{-1} \text{ cm}^{-2} \text{ \AA}^{-1}, \quad (1)$$

where F_{λ} is the spectral flux density and λ is the wavelength. The power-law limit is shown in Figures 3 and 6 and is included in Table 3. We note that the limits from spectra are more constraining than image limits at corresponding frequencies.

4.4. X-Ray Limits

X-ray limits on the compact object are set using the 2015 September 17 *Chandra*/ACIS observation and the ejecta absorption estimate from the SN model B15 (Appendix C). We investigate the standard blackbody model, the XSPEC thermal model *nsmxg* (Mori & Ho 2007; Ho et al. 2008), and two power laws with photon indices (Γ) of 1.63, corresponding to the Crab Pulsar, and 2.108, corresponding to the Crab Nebula (Willingale et al. 2001). The *nsmxg* model describes thermal emission from an NS for different atmospheric compositions and magnetic field strengths. We only explore the case of a NS with a carbon atmosphere and a magnetic field strength of 10^{12} G . A carbon-atmosphere model was reported to fit the NS in Cas A (Ho & Heinke 2009; Posselt et al. 2013). See Figure 2 of Ho & Heinke (2009) for a comparison of different atmospheric compositions. Apart from the spread light fraction, only the temperature is allowed to vary for the two thermal components and the normalization for the two power laws. The remaining parameters are frozen under the assumptions (discussed in Section 5.3.1) of a gravitational mass of $1.4 M_{\odot}$, local (unredshifted) NS radius of 10 km, and uniform emission from the entire surface. The assumed mass and radius give a gravitational redshift factor of 0.766.

All X-ray limits are listed in Table 4. The presented effective surface temperatures (T) are given in the local (unredshifted) frame. The parameter (K_{∞}) is the XSPEC power law normalization and is given in the observed frame (“at infinity”). The luminosities (L_{∞}) are also given in the observed frame to facilitate comparisons with other observational studies. The luminosities for the thermal components are bolometric, whereas the power-law luminosities are given for the observed 2–10 keV range.

The limits for the standard blackbody and the $\Gamma = 1.63$ power law are given for three different levels of SN ejecta absorption. The selected amounts are the average, 10th percentile, and 90th percentile of the optical depth. The general trends for the two thermal components and the two power laws

Table 3
UVOIR Limits

Instrument	Filter/Grating	Method	Epoch ^a (YYYY mm dd)	Wavelength (Å)	Flux Density (erg s ⁻¹ cm ⁻² Å ⁻¹)	Luminosity (erg s ⁻¹)	Luminosity (L _⊙)
WFC3	F225W	Spatial	2009 Dec 13	2150–2615	4.0×10^{-17}	5.8×10^{33}	1.5
WFC3	F336W	Spatial	2009 Dec 13	3102–3617	9.5×10^{-18}	1.5×10^{33}	0.40
WFC3	F438W	Spatial	2009 Dec 12	4026–4638	8.4×10^{-18}	1.6×10^{33}	0.42
WFC3	F555W	Spatial	2009 Dec 13	4556–6112	6.7×10^{-18}	3.3×10^{33}	0.86
WFC3	F625W	Spatial	2009 Dec 12	5525–6991	6.7×10^{-18}	3.1×10^{33}	0.81
WFC3	F841W	Spatial	2009 Dec 13	7284–8864	2.8×10^{-18}	1.4×10^{33}	0.36
WFC3	F110W	Spatial	2011 Jan 05	9203–13901	6.0×10^{-18}	8.8×10^{33}	2.3
WFC3	F160W	Spatial	2011 Jan 05	14027–15925	4.5×10^{-18}	2.7×10^{33}	0.70
WFC3	F438W	Spatial	2015 May 24	4022–4639	7.1×10^{-18}	1.4×10^{33}	0.36
WFC3	F625W	Spatial	2015 May 24	5529–6982	5.5×10^{-18}	2.5×10^{33}	0.65
NACO	<i>H</i>	Spatial	2010 Oct 26	14950–18250	7.6×10^{-19}	7.9×10^{32}	0.21
NACO	<i>K_s</i>	Spatial	2012 Dec 14	20050–23550	2.1×10^{-19}	2.3×10^{32}	0.061
STIS	G750L	Spectral	2014 Aug 16	5300–10000	1.5×10^{-18b}	2.3×10^{33}	0.59
SINFONI	...	Spectral	2014 Oct 10	15150–15800	2.4×10^{-19}	5.0×10^{31}	0.013
SINFONI	...	Spectral	2014 Oct 10	16900–18125	1.4×10^{-19}	5.3×10^{31}	0.014
SINFONI	<i>H</i>	Spectral	2014 Oct 10	15000–18500 ^c	1.8×10^{-19}	2.0×10^{32}	0.051
SINFONI	...	Spectral	2014 Oct 12	19875–22725	1.8×10^{-19}	1.6×10^{32}	0.043
SINFONI	...	Spectral	2014 Oct 12	22725–23825	1.2×10^{-19}	4.2×10^{31}	0.011
SINFONI	<i>K</i>	Spectral	2014 Oct 12	19500–24000 ^c	1.7×10^{-19}	2.3×10^{32}	0.061

Notes.^a Start of first exposure if the observation is multi-day.^b Average of the limiting power law.^c Extrapolated slightly outside of, and interpolated between, fitted intervals.

are the same; the difference between the 10th and 90th percentiles is a factor of ~ 2 in luminosity for the thermal components and ~ 3 for the power laws. Absorption by the ISM is always included, but we also provide limits for no SN ejecta absorption. This represents the minimum amount of absorption, in case the SN explosion model describes SN 1987A poorly and we happen to have a very favorable line of sight.

The reason for the extremely high limiting temperatures and luminosities of the thermal models is that the high optical depths at energies below ~ 4 keV effectively absorb all emission. We point out that an important factor to the thermal components crossing the detection threshold is the shift of the emission toward higher energies where the optical depth is lower. The power-law models are more constrained in the sense that the limiting luminosity in the 2–10 keV range is much lower because the power-law components extend to higher energies.

4.5. Bolometric Limit

The bolometric luminosity of the compact object can be constrained by the total energy budget of SN 1987A. The energy inputs are radioactive decay of ^{44}Ti and the unknown contribution from the compact object. The energy outputs are far-infrared (FIR) dust emission and UVOIR de-excitation and recombination emission lines. Detailed models of SN 1987A predict that much of the emission powered by ^{44}Ti would emerge as fine structure lines in MIR (Jerkstrand et al. 2011), but observations severely constrain these lines (Lundqvist et al. 2001; Bouchet et al. 2006). This implies that the MIR emission is reprocessed and escapes as thermal dust emission in the submillimeter to FIR (Matsuura et al. 2011, 2015; Indebetouw et al. 2014; Dwek & Arendt 2015).

The lifetime of ^{44}Ti is $\tau = 85.0$ years (half-life of 58.9 years, Ahmad et al. 2006) and decays into ^{44}Sc , which emits 596-keV

positrons when promptly decaying to stable ^{44}Ca . All positrons deposit their energy locally under the assumption of the presence of a weak magnetic field (Ruiz-Lapuente & Spruit 1998) and a fraction f_h of the energy goes into heating and the rest goes into excitation and ionization (Kozma & Fransson 1992; Jerkstrand et al. 2011). We assume that the ionization fraction is slightly higher at $\sim 10,000$ days (current epochs) than at 2875 days, which is what was modeled by Jerkstrand et al. (2011). A higher ionization fraction results in a higher heating fraction (Figure 5 of Kozma & Fransson 1992).

The emission processes relevant for the compact object are thermal surface emission, accretion, or pulsar wind activity. We assume that the emission is dominated by X-ray emission below 10 keV, which is absorbed locally because of the high optical depth (Alp et al. 2018) and escapes as thermal dust emission or UVOIR lines. Both surface emission and accretion would be observed as unresolved point sources. Chevalier & Fransson (1992) investigated the early evolutions of young pulsars and their effect on the surrounding ejecta and found that the bubble expansion velocity is $\sim 500\text{--}800$ km s⁻¹ for a pulsar luminosity of 10^{39} erg s⁻¹ above 13.6 eV. The current limits on the compact object constrains the luminosity, and consequently the expansion velocity, to be orders of magnitude lower. For expansion velocities less than ~ 100 km s⁻¹, it is reasonable to treat a possible pulsar wind nebula (PWN) as a point source. Assuming the compact object to be point-like allows us to separate the cases where the line of sight is free of dust and dust-obscured, and use the point-source image limits in the dust-free case.

In the case where our line of sight is free of dust, we assume that 70% of the input from the compact object goes into heating and the remaining 30% escapes as UVOIR emission lines. These fractions are distinct from those for the positron input, but we assume them to be the same (Kozma & Fransson 1992; Jerkstrand et al. 2011). We do not consider further reprocessing

Table 4
X-Ray Limits

Model	Absorption	χ^2	d.o.f.	$\chi^2/\text{d.o.f.}$	f_s^a (10^{-2})	T^b (MK)	Γ^c	K_∞^b ($10^{-4} \text{ keV}^{\Gamma-1} \text{ s}^{-1} \text{ cm}^{-2}$)	L_∞^d (erg s^{-1})
Blackbody	No SN abs.	28.6	26	1.10	5.0 ± 0.3	4.4	1.6×10^{35}
Blackbody	10th percentile	29.8	26	1.15	5.9 ± 0.3	8.2	1.9×10^{36}
Blackbody	Average	29.4	26	1.13	5.9 ± 0.3	8.9	2.6×10^{36}
Blackbody	90th percentile	29.1	26	1.12	6.0 ± 0.3	9.6	3.6×10^{36}
Carbon atm.	Average	29.0	26	1.12	6.0 ± 0.3	7.7	1.5×10^{36}
Power law	No SN abs.	29.7	26	1.14	5.6 ± 0.3	...	1.63	2.9	4.1×10^{34}
Power law	10th percentile	29.1	26	1.12	6.0 ± 0.3	...	1.63	2.1	3.0×10^{35}
Power law	Average	28.9	26	1.11	6.0 ± 0.3	...	1.63	3.5	4.9×10^{35}
Power law	90th percentile	29.1	26	1.12	6.0 ± 0.3	...	1.63	6.1	8.8×10^{35}
Power law	Average	28.9	26	1.11	6.0 ± 0.3	...	2.108	7.7	5.3×10^{35}

Notes.

^a The fraction of spread light from the ER at the limiting values of the parameter of interest (either T or K_∞). This can be compared to the predicted value of $0.073_{-0.005}^{+0.011}$ (Section 3.6.3). Uncertainties are 1σ .

^b 3σ upper limits.

^c Frozen during fits.

^d Observed bolometric luminosity for the thermal components. Luminosity in the observed 2–10 keV range for the power laws.

of the energy that goes into heating, which most likely escapes as thermal dust emission (Bouchet et al. 2006; Jerkstrand et al. 2011). The compact object is situated in the central regions where the photoabsorption is dominated by iron (Figure 2 of Alp et al. 2018), which implies that the line spectrum of the reprocessed emission from the compact object could be different from that of the ^{44}Ti -powered ejecta. Therefore, we choose a conservative limit on the reprocessed UVOIR emission from the compact object to be $4 \times 10^{-17} \text{ erg s}^{-1}$ in the range 1000–3000 Å, which is an extrapolation of the 3σ UV (F225W) *HST* point-source limit (Section 4.2 and Figure 6). This spectral shape was chosen because it results in the least constraining limit. The wavelength range covers the region where many of the metal lines are expected to escape (Figures 3–5 of Jerkstrand et al. 2011) and longer wavelengths are strongly constrained by the limits (Figure 6 and Table 3). The flux limit corresponds to an allowed UVOIR luminosity of $6.6 L_\odot$, which for the assumed heating fraction of 70% results in a bolometric limit of $22 L_\odot$. The epoch of this limit is 2009 December, which is set by the *HST* UV observation.

The situation is different in the case where our line of sight to the compact object is obscured by dust. In this case, the contribution from the compact object is added to the contribution to dust heating from ^{44}Ti . Out of the fraction $1 - f_h$ of the positron input that goes into excitation and ionization, a fraction f_d is absorbed by dust. The case is simpler for the electromagnetic input from the compact object, all of which goes into dust heating in the dust-obscured case. This implicitly assumes spherical symmetry and means that the total dust luminosity is expected to be

$$L_d = [f_h + f_d (1 - f_h)] L_{\text{Ti}} + L_*, \quad (2)$$

where L_{Ti} is the ^{44}Ti positron decay luminosity and L_* is the contribution from the compact object.

A limit on L_* can now be determined. The values of the other parameters are taken to be $L_d = 295 \pm 17 L_\odot$ (Dwek & Arendt 2015; Matsuura et al. 2015, weighted values from 2010 and 2012, and scaled to 51.2 kpc), $L_{\text{Ti}} = 298 \pm 36 L_\odot$ (initial ^{44}Ti mass of $1.6 \times 10^{-4} M_\odot$ for 51.2 kpc, Jerkstrand et al. 2011; Boggs et al. 2015), $f_h = 0.55\text{--}0.85$ (Kozma & Fransson 1992;

Jerkstrand et al. 2011), and $f_d = 0.5\text{--}0.7$ (Lucy et al. 1989, 1991; Wooden et al. 1993; Wang et al. 1996; Fassia et al. 2002; Jerkstrand et al. 2011, see also Section 4.1). The values are scaled to 9090 days after explosion (2012 January), which is the time of the dedicated *Herschel* observations of the dust luminosity (Matsuura et al. 2015). The distributions are assumed to be Gaussian and confidence intervals are 1σ except for the fractions, which are assumed to be uniformly distributed within the intervals. This is clearly a very primitive model but the uncertainty in the Ti mass estimate is the largest source of uncertainty and an improvement in the determination of L_{Ti} in the near future is unlikely. Therefore, a more detailed model of the energy budget would not improve the limit on L_* by much. Following the above reasoning, the estimate of the compact object luminosity is $L_* = 33_{-38}^{+37} L_\odot$, which shows that an additional contribution from the compact object is not statistically significant. The 3σ upper limit is $L_* < 138 L_\odot$.

Some simplifications have implicitly been made. It is possible that some fraction of the energy emitted by the compact object escapes the remnant before being reprocessed into observable wavebands, such as, for example, in the MIR (Section 5.7.1, Bouchet et al. 2006; Bouchet & Danziger 2014) or as high-energy gamma-rays (Section 5.7.2). The X-ray emission from the ring provides an additional energy source for the ejecta (Larsson et al. 2011), but this primarily affects the outer H and He envelope (Fransson et al. 2013; Larsson et al. 2013).

5. Discussion

All limits on the compact object in SN 1987A presented in Section 4 apply to both NSs and BHs. However, the expected emission characteristics for the two classes of objects are very different. This discussion primarily focuses on NSs because most studies favor the creation of an NS in SN 1987A (Section 1) and NSs power a wider diversity of physical processes. In contrast, BHs primarily reveal themselves through accretion, which is explored in Section 5.3.2 and more comprehensively in Graves et al. (2005).

Table 5 summarizes all limits on physical parameters. The combination of all available information favors that the

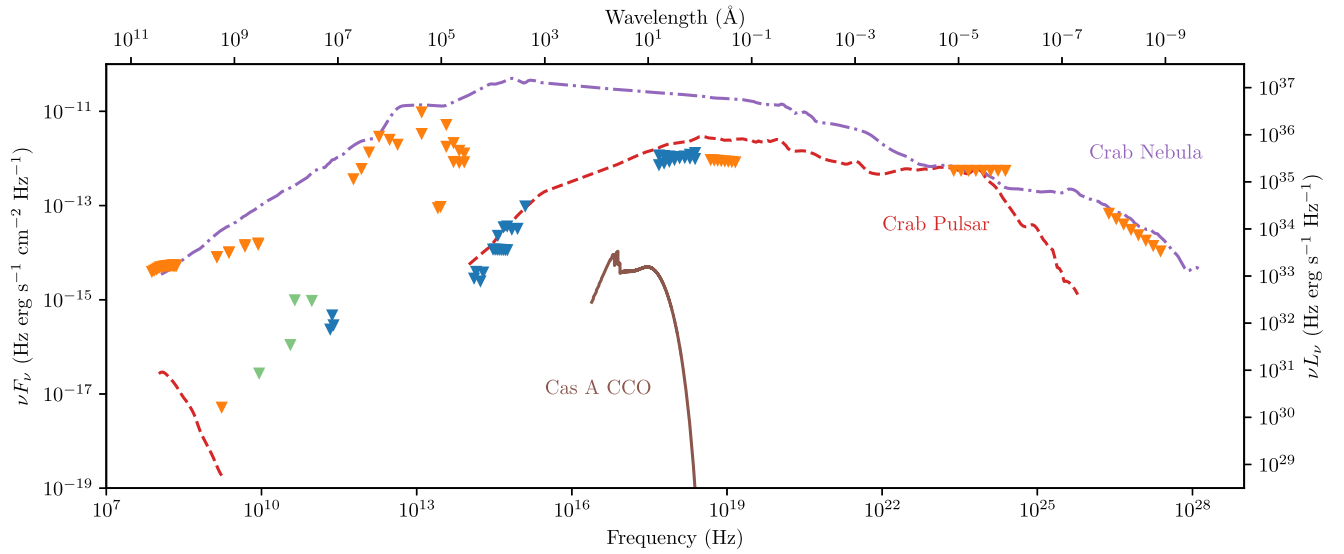


Figure 7. Limits (triangles) on the compact object in SN 1987A, shown together with the spectra of the Crab Nebula (dashed–dotted purple line; Bühler & Blandford 2014, and references therein), the Crab Pulsar (dashed red line; Bühler & Blandford 2014, and references therein), and the CCO in Cas A modeled as a NS with a carbon atmosphere (solid brown line; Posselt et al. 2013). The spectra are scaled to the distance of SN 1987A. The blue limits are from this work, and the orange and green limits are from the literature. The green limits are super-resolved using deconvolution algorithms and all orange limits are unresolved except for the VLBI observation at 1.7 GHz and the Gemini/T-ReCS observations at 10 μm .

Table 5
Model-dependent Constraints on Physical Parameters

Model	Method ^a	Observation ^b	Dust ^c	Spectrum	Lum. (L_{\odot})	Limit on Physical Parameters
NS Surface	DO	<i>Chandra</i>	...	Thermal	450	$T < 8 \text{ MK}$ ($T_{\infty} < 6 \text{ MK}$)
NS Surface	EB	<i>HST F225W</i>	N	Thermal	22	$T < 3.8 \text{ MK}$ ($T_{\infty} < 2.9 \text{ MK}$)
NS Surface	EB	<i>Herschel</i>	Y	Thermal	138	$T < 5.9 \text{ MK}$ ($T_{\infty} < 4.5 \text{ MK}$)
Accretion	DO	<i>Chandra</i>	...	X-ray dominated	300	$\dot{M} < 2.0 \times 10^{-11} \eta^{-1} M_{\odot} \text{ yr}^{-1}$
Accretion	EB	<i>HST F225W</i>	N	X-ray dominated	22	$\dot{M} < 1.5 \times 10^{-12} \eta^{-1} M_{\odot} \text{ yr}^{-1}$
Accretion	EB	<i>Herschel</i>	Y	X-ray dominated	138	$\dot{M} < 9.2 \times 10^{-12} \eta^{-1} M_{\odot} \text{ yr}^{-1}$
PWN	DO	SINFONI 1.7 μm	N	Crab Nebula	3	$B < 1.8 \times 10^{13} P^2 \text{ G s}^{-2}$
PWN	DO	ALMA 213 GHz	...	Crab Nebula	10	$B < 3.2 \times 10^{13} P^2 \text{ G s}^{-2}$
PWN	DO	SINFONI 1.7 μm	N	Crab Pulsar	528	$B < 2.3 \times 10^{14} P^2 \text{ G s}^{-2}$
PWN	DO	<i>Chandra</i>	...	Crab Pulsar	830	$B < 2.9 \times 10^{14} P^2 \text{ G s}^{-2}$
PWN	EB	<i>HST F225W</i>	N	X-ray dominated	22	$B < 4.7 \times 10^{13} P^2 \text{ G s}^{-2}$
PWN	EB	<i>Herschel</i>	Y	X-ray dominated	138	$B < 1.2 \times 10^{14} P^2 \text{ G s}^{-2}$

Notes.

^a Either constrained by direct observations (DO) or by the energy budget (EB).

^b Which observation is constraining. *Herschel* observations (Dwek & Arendt 2015; Matsuura et al. 2015) are used for the bolometric limit (Section 4.5).

^c Ejecta dust along the line of sight: Yes, No, or blank if limit is insensitive to dust.

compact object is a dust-obscured thermally emitting NS (Section 5.7). The discussion is organized as follows. We compile literature limits for a comprehensive overview of SN 1987A observations across the entire electromagnetic spectrum in Section 5.1 and compare our limits with previous works in Section 5.2. The implications of the limits based on direct observations for thermal surface emission are discussed in Section 5.3.1, accretion is discussed in Section 5.3.2, and pulsar activity is discussed in Section 5.3.3. We relate the bolometric limit to physical parameters in Section 5.4 and extrapolate the limits to other epochs using simple models in Section 5.5. Lastly, we explore constraints on a possible binary main-sequence companion in Section 5.6, remaining possibilities for the compact object in Section 5.7, and briefly look into future prospects in Section 5.8.

5.1. Global Limits

Limits on a point source collected from the literature are included to give a complete coverage over the entire electromagnetic spectrum. We only include literature limits at frequencies not covered by this work. Limits covering the same bands as our limits are instead discussed in Section 5.2. An overview of limits at all frequencies is shown in Figure 7. More details on the literature limits are provided in Table 6. We categorize the limits based on the methods employed. Unresolved imaging in this context implies that the ER and ejecta are not spatially resolved. These limits are just the total flux of the ER and ejecta combined, resulting in very conservative limits. The unresolved radio limit is dominated by ejecta-ER interactions (Callingham et al. 2016), unresolved IR limits by thermal dust emission (Matsuura et al. 2015;

Table 6
Literature Limits on SN 1987A

Frequency (Hz)	Flux Density ($\text{erg s}^{-1} \text{cm}^{-2} \text{Hz}^{-1}$)	Epoch ([YYYY–YYYY])	Instr. ^a	Resolution ^b	Conf. Level ^c	References
$(0.076\text{--}8.642) \times 10^9$	$(5.1\text{--}0.17) \times 10^{-23}$	2013–2014	MWA, ATCA	U	...	Callingham et al. (2016)
1.7×10^9	0.3×10^{-26}	2008	VLBI	R	$3\text{-}\sigma$	Ng et al. (2011)
9×10^9	0.3×10^{-26}	1996 ^d	ATCA	S	$3\text{-}\sigma$	Ng et al. (2008)
36.2×10^9	$0.3 \pm 0.2 \times 10^{-26}$	2008	ATCA	S	E	Potter et al. (2009)
44×10^9	2.2×10^{-26}	2011	ATCA	S	E	Zanardo et al. (2013)
94×10^9	1×10^{-26}	2011	ATCA	S	$2\text{-}\sigma$	Lakićević et al. (2012b)
$(0.6\text{--}4.3) \times 10^{12}$	$(50\text{--}150) \times 10^{-26}$	2012	SPIRE, PACS	U	...	Matsuura et al. (2015)
$(12\text{--}83) \times 10^{12}$	$(1.0\text{--}76) \times 10^{-26}$	2003–2015	MIPS, IRAC	U	...	Arendt et al. (2016)
26×10^{12}	0.34×10^{-26}	2005	T-ReCS	R	$3\text{-}\sigma$	Bouchet et al. (2006)
29×10^{12}	0.32×10^{-26}	2003	T-ReCS	R	E ^e	Bouchet et al. (2004)
$(0.5\text{--}1.5) \times 10^{19}$	$(1.9\text{--}0.6) \times 10^{-31}$	2010–2011	IBIS	U	...	Grebenev et al. (2012)
$(2.4\text{--}24.2) \times 10^{23}$	$(2.2\text{--}0.22) \times 10^{-36}$	2008–2014	LAT	U	...	Ackermann et al. (2016)
$(2.4\text{--}24.2) \times 10^{26}$	$(2.8\text{--}0.04) \times 10^{-40}$	2003–2012	HESS	U	...	H.E.S.S. Collaboration et al. (2015)

Notes.

^a The abbreviations and acronyms are as follows: Murchison Widefield Array (MWA); Australia Telescope Compact Array (ATCA); Very Long Baseline Interferometry (VLBI) using ATCA, Parkes, Mopra, and the NASA DSS 43 antenna at Tidbinbilla; Spectral and Photometric Imaging Receiver (SPIRE) and Photodetector Array Camera and Spectrometer (PACS) on board *Herschel*; Multiband Imaging Photometer (MIPS) and Infrared Array Camera (IRAC) on board *Spitzer*; Thermal Region Camera and Spectrograph (T-ReCS) attached to the Gemini South 8 m Telescope; Imager on board the *INTEGRAL* Satellite (IBIS) on board *INTEGRAL*; The Large Area Telescope (LAT) on board *Fermi*; and the High Energy Stereoscopic System (HESS).

^b Either unresolved (U), meaning that the flux densities are given for the ER and ejecta combined; super-resolved (S), meaning that images are restored using a deconvolution algorithm; or resolved (R), meaning that the ER and central ejecta structure are spatially resolved.

^c Flux densities presented as estimates of a point source rather than upper limits are denoted by “E.” This is left blank for values presented as measured fluxes of the ejecta and ER combined.

^d Limits from other epochs are very similar.

^e This was reported as potential dust emission.

Arendt et al. (2016), unresolved X-ray limits most likely by ejecta-ER interactions (Grebenev et al. 2012), and gamma-ray limits most likely by spread light from the nearby objects N 157B and 30 Dor C (H.E.S.S. Collaboration et al. 2015; Ackermann et al. 2016). Super-resolved implies that images are restored using a deconvolution algorithm, which introduces additional assumptions and is model-dependent in some cases. This is especially unreliable because the compact object is surrounded by bright ejecta (e.g., White 1994). Resolved images clearly distinguish the ER from the central ejecta and are the most robust measurements. The VLT/SINFONI, *HST*/STIS, and *Chandra*/ACIS limits from this work are based on spectra, whereas all other limits are determined using images.

The radio limits of Potter et al. (2009) and Zanardo et al. (2013) in Table 6 are referred to as estimates. These are excess sources inside the ER that were interpreted as possible indications of a pulsar. However, the evidence remains inconclusive and we are not able to compare our limits with their observations.

5.2. Comparison with Previous Limits

Earlier studies have presented limits on the compact object in SN 1987A in (sub-)mm, optical, UV, and X-rays. Zanardo et al. (2014) discussed the possibility of a PWN with a flux of 3 mJy in the range 102–672 GHz. This is not directly comparable to our limits of ~ 0.1 mJy at 213–247 GHz because our limits apply to point sources and a PWN might be spatially extended (cf. Figure 5).

Graves et al. (2005) placed limits in optical and UV using data from *HST*. The image limits from Graves et al. (2005) are lower than ours by approximately a factor of 2, but the STIS

limit presented in this work is $\sim 30\%$ more constraining than any previous limit in the same wavelength range. There are numerous factors that contribute to the differences. Their STIS spectrum is from 1999 December and images are from 2003 November taken by the Advanced Camera for Surveys (ACS), which has a higher angular resolution than WFC3. Our observations are from later epochs, which implies that the ejecta have expanded significantly, the shock interactions with the ER have evolved, the ER X-ray illumination has increased (Larsson et al. 2011), and our search region needs to be larger. Additionally, slightly different values for the reddening and equivalent widths of the filters are used, as well as a different search algorithm (Appendix B). We verified that the combined effect of all factors explains the differences between our limits and those of Graves et al. (2005).

Many authors have presented upper limits on the X-ray luminosity of the compact object in SN 1987A using observations from *Chandra* and *XMM-Newton* (Burrows et al. 2000; Park et al. 2002, 2004; Shtykovskiy et al. 2005; Haberl et al. 2006; Ng et al. 2009; Orlando et al. 2015; Frank et al. 2016; Esposito et al. 2018). The reported luminosity limits are in the range $(0.3\text{--}60) \times 10^{34} \text{ erg s}^{-1}$ for different instruments, methods, assumed spectra, and energy ranges (often 2–10 keV). This should be compared to our limit of $4 \times 10^{34} \text{ erg s}^{-1}$ for the $\Gamma = 1.63$ power-law model without ejecta absorption (Table 4). However, most of our X-ray limits are approximately an order of magnitude less constraining than previous X-ray limits because we use a more realistic model of the soft X-ray photoabsorption of the SN ejecta based on 3D neutrino-driven SN explosion models (Alp et al. 2018). We also employ a method (Section 3.6) that uses the angular

resolution of *Chandra*/ACIS in conjunction with its spectral resolution.

5.3. Model Comparisons

5.3.1. Thermal Emission

The direct limits do not strongly constrain the surface temperature of an NS (Tables 4 and 5). The remainder of this section provides the information needed to draw this conclusion. We note that more constraining limits are obtained from the bolometric limits (Sections 5.4 and 5.7).

To relate the surface temperature of an NS to observed luminosity, it is necessary to adopt a mass and radius. We assume a gravitational mass of $1.4 M_{\odot}$ and a local (unredshifted) radius of 10 km for an NS in SN 1987A. Recent best estimates based on Bayesian analyses of low-mass X-ray binaries (Steiner et al. 2013), nuclear physics and observational constraints on the NS equation of state (Hebeler et al. 2013), and the binary NS merger GW170817 (Bauswein et al. 2017) favor radii in the range 11–13 km; see also Figure 10 of Özel & Freire (2016). The primary reason for choosing a radius of 10 km is that the limits are more conservative because all reported temperature limits decrease for an increasing NS radius and fixed mass. The decrease in limiting temperature for a radius of 12 km is approximately a factor of 0.89 for T and 0.94 for T_{∞} , because of the different dependencies on the gravitational redshift factor.

Typical surface temperatures of young NSs are of the order of a few million Kelvin and correspond to spectral peaks at soft X-ray energies of ~ 1 keV. The characteristic temperature for a given NS age depends on the relatively unknown cooling properties of NSs (Yakovlev & Pethick 2004). For an NS at 30 years that has not undergone thermal relaxation, a typical temperature is $T \approx 3.3$ MK ($T_{\infty} \approx 2.5$ MK, Gnedin et al. 2001; Shternin & Yakovlev 2008; Page et al. 2009; Klochkov et al. 2015). A more extreme case is for an NS with a carbon heat blanket. Carbon is more heat transparent and gives $T \approx 4.1$ MK ($T_{\infty} \approx 3.2$ MK, Yakovlev et al. 2011; Klochkov et al. 2015). These values are at the high end of temperatures predicted for an NS in SN 1987A. If thermal relaxation has started, the temperature would decrease quickly at current epochs (Gnedin et al. 2001; Yakovlev & Pethick 2004; Shternin & Yakovlev 2008; Page et al. 2009).

Limits on thermal emission from an NS in SN 1987A based on the X-ray observation are provided in Tables 4 and 5. The X-ray limits constrain thermal spectra much more strictly than the UVOIR limits. The limiting temperatures are approximately 8 MK for all expected levels of ejecta absorption and NS atmospheres. This is clearly above the predicted values of $T \lesssim 4$ MK, implying that the direct observations do not exclude any models. Thus, a scenario where SN 1987A created a central compact object (e.g., Posselt et al. 2013; Bogdanov 2014) is consistent with the observational limits.

5.3.2. Accretion

It is possible that the compact object is accreting a significant amount of matter. An extensive study of many different accretion scenarios was made by Graves et al. (2005, their Sections 5 and 6), to which the reader is referred for a comprehensive analysis of accretion in SN 1987A. We restrict our discussion of accretion to the simplest model with the

purpose of estimating the luminosity, and find that most predictions for fallback are excluded unless the accretion efficiency is less than 0.03 (cf. Section 5.5).

The simplest accretion model is to assume that a significant amount of the gravitational binding energy of the infalling material is converted into radiation. The accretion luminosity (L_a) is then given by

$$\begin{aligned} L_a &= \eta \dot{M} c^2 \\ &= 5.7 \times 10^{46} \eta \left(\frac{\dot{M}}{M_{\odot} \text{ yr}^{-1}} \right) \text{ erg s}^{-1}, \end{aligned} \quad (3)$$

where η is the accretion efficiency, \dot{M} is the accretion rate, and c is the speed of light in vacuum. A typical accretion efficiency is $\eta \approx 0.1$ for an NS of mass $1.4 M_{\odot}$ and radius 10 km, assuming the accreted gas radiatively cools efficiently (e.g., McCray 1979). The efficiency of accretion onto BHs is more model-dependent. Possible values of BH accretion efficiencies range from 10^{-10} for spherically symmetric accretion (Shapiro 1973) to 0.4 for disk accretion (Frank et al. 2002). For reference, the Eddington luminosity (L_{Edd}) for an object of mass $1.4 M_{\odot}$ is $1.8 \times 10^{38} \text{ erg s}^{-1}$, which corresponds to an Eddington accretion rate (\dot{M}_{Edd}) of $3.1 \times 10^{-9} \eta^{-1} M_{\odot} \text{ yr}^{-1}$. This relies on some standard assumptions that are inapplicable in this case, but we choose to use the Eddington luminosity as a unit for comparison with other works.

The amount of fallback onto NSs after SN explosions has been estimated to $\lesssim 0.1 M_{\odot}$, which mostly accrete on timescales of $\lesssim 1$ year (Chevalier 1989; Houck & Chevalier 1991; Brown & Weingartner 1994; Chatterjee et al. 2000). Brown & Weingartner (1994) estimated that a mass of 10^{-4} – $10^{-3} M_{\odot}$ remains bound to the NS in SN 1987A after ~ 3 years. Relevant timescales for accretion of this remaining mass are $\gtrsim 1000$ years, and it is possible that most of the remaining mass is expelled (Houck & Chevalier 1991; Chatterjee et al. 2000). As an example, we assume a relatively conservative fallback mass of $10^{-5} M_{\odot}$ that is uniformly accreted over 10^4 yr. This results in an accretion rate of $10^{-9} M_{\odot} \text{ yr}^{-1}$, which corresponds to $L_a = 6 \times 10^{37} \eta \text{ erg s}^{-1}$ ($\approx 10^4 \eta L_{\odot}$, Equation (3)).

The X-ray limits are 0.04– $3.6 \times 10^{36} \text{ erg s}^{-1}$ (Table 4) at 10,433 days (2015 September). Given that the spectrum is not known, $\dot{M} < 2 \times 10^{-11} \eta^{-1} M_{\odot} \text{ yr}^{-1}$ ($\approx 10^{36} \text{ erg s}^{-1} \approx 6 \times 10^{-3} \dot{M}_{\text{Edd}}$) can be taken as a limit on the current accretion rate in SN 1987A based on the X-ray observation. This is only consistent with the prediction of $6 \times 10^{37} \eta \text{ erg s}^{-1}$ if η is < 0.03 . The discrepancy between models and observations is even clearer if the temporal evolution of the accretion rate is considered (Section 5.5).

5.3.3. Magnetic Field and Rotation

We constrain the surface magnetic field strength (B) and rotational period (P) of an NS in SN 1987A using a simple model of a rotation-powered PWN and assuming spectra in the form of the Crab Nebula and Pulsar. An analog of the Crab Nebula or the Crab Pulsar in SN 1987A is ruled out even if our line of sight is dust-obscured (Table 5).

The total luminosity of an NS can be modeled by a rotating magnetic dipole in vacuum (e.g., Equation (10.5.4) of

Shapiro & Teukolsky 1983):

$$L = \frac{2^5 \pi^4 B^2 R^6}{3 c^3 P^4} = 3.9 \times 10^{31} \left(\frac{B}{10^{12} \text{ G}} \right)^2 \left(\frac{P}{\text{s}} \right)^{-4} \left(\frac{R}{10 \text{ km}} \right)^6 \text{ erg s}^{-1}. \quad (4)$$

Several assumptions have implicitly been made; the rotation axis and the magnetic dipole axis are orthogonal and the dominating source of energy is the rotational energy of the NS. We follow the convention of letting the “surface” magnetic field strength be the magnetic equator field strength and using the vacuum formula (e.g., the ATNF Pulsar Catalogue, Manchester et al. 2005). The magnetic field strength at the magnetic poles is a factor of two higher. We also note that the force-free magnetic dipole formula would imply 1.7 times lower magnetic field strengths than the vacuum formula for orthogonal rotation and magnetic axes (Spitkovsky 2006). In the simplest picture, the energy emitted by the NS is deposited into the surroundings where it is reprocessed. We do not attempt to model the complex interactions that generate the observed spectrum of a PWN. Instead, we assume that the deposited energy emerges with the spectrum of the Crab Nebula or the Crab Pulsar, and study these two cases separately. The spectrum of the pulsar is the pulsed component, which corresponds to radiation originating predominantly from the immediate surroundings of the pulsar and to a lesser extent from the pulsar itself. The Crab is one of the most extreme sources in the sky and it is not a typical PWN. For a high-energy comparison of the pulsed emission, see Figure 28 of Kuiper & Hermsen (2015), and for a multiwavelength comparison of the Crab and PSR B0540-69.3, see Figure 15 of Serafimovich et al. (2004). However, the Crab is relatively young, well-observed, and frequently used as a reference. The physical scenario is that an NS created by SN 1987A is a pulsar that drives a younger and smaller analog of the Crab in the SN remnant.

With Equation (4) and a spectral shape, we can compute the region in the BP -plane that is allowed by the upper limits. This is done by taking the Crab Nebula spectrum and the Crab Pulsar spectrum, scaling to the distance of SN 1987A, and then scaling the spectra such that they are consistent with the limits (see Figure 7). If our line of sight is free of dust, both spectra are constrained by the SINFONI data point at $1.7 \mu\text{m}$, otherwise the nebula spectrum is constrained by the 213 GHz limit and the pulsar spectrum is constrained by the $\Gamma = 1.63$ X-ray power-law limit. We only use the new limits presented in this work and we assume that a PWN is point-like (Section 4.5, and Chevalier & Fransson 1992). The allowed luminosities vary from $3 L_\odot$, corresponding to 8.2×10^{-5} of the Crab Nebula, to $830 L_\odot$, corresponding to 0.42 of the Crab Pulsar (Table 5). The luminosities can be translated to limits in the BP -plane by rearranging Equation (4). The local (unredshifted) radius is taken to be 10 km. The limits span a range from $B < 1.8 \times 10^{13} P^2 \text{ G s}^{-2}$ to $B < 2.9 \times 10^{14} P^2 \text{ G s}^{-2}$, and are included in Table 5 and shown in Figure 8. The limits are all relatively low and any possible PWN activity is most likely very weak.

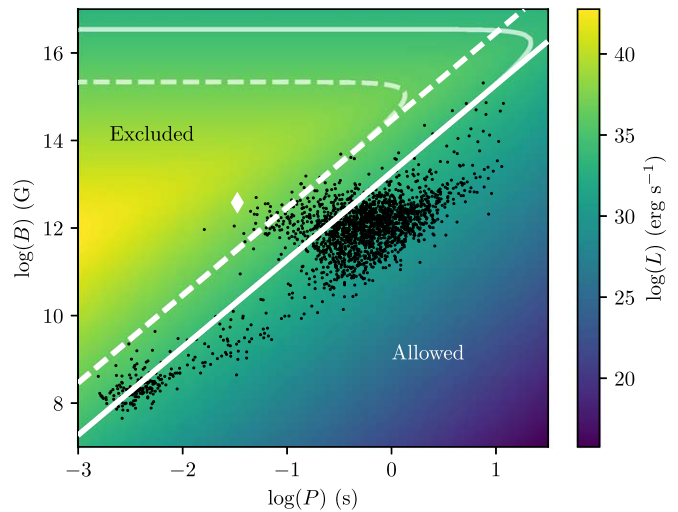


Figure 8. Limits on B and P of an NS in SN 1987A, together with the pulsars (black points) in the ATNF Pulsar Catalogue (Manchester et al. 2005), which are included for reference and do not represent the expected properties of the compact object in SN 1987A. The large white diamond is the Crab Pulsar. The solid line is the limit from direct observations for a Crab Nebula spectrum in the dust-free case and the dotted line is for a Crab Pulsar spectrum obscured by dust. These limits are chosen because they are the two extremes, implying that all other BP -plane limits are covered within the range. The shaded extensions that are partially horizontal correspond to the respective lines but for constraints on birth values of B and P for an assumed temporal evolution (see Section 5.5). The color map represents the current luminosity of a rotating dipole in vacuum as modeled by Equation (4) as a function of birth values of B and P .

5.4. Energy Budget

The bolometric limit on the compact object in SN 1987A is $22 L_\odot$ at 8329 days (2009 December) if our line of sight is free of dust and $138 L_\odot$ at 9090 days (2012 January) in the dust-obscured case. The limits rely on many assumptions (Section 4.5) and the direct observations are arguably less model-dependent. The direct-observation limits and the bolometric limits can be viewed as independent limits on the compact object in SN 1987A. All constraints on physical parameters are provided in Table 5. Only the bolometric limits on the effective temperature are substantially more constraining than the corresponding direct-observation limits.

In the dust-free case, the bolometric limit constrains the blackbody temperature to $T < 3.8 \text{ MK}$ ($T_\infty < 2.9 \text{ MK}$) for an NS radius of 10 km and mass of $1.4 M_\odot$. The corresponding value for the dust-obscured case is $T < 5.9 \text{ MK}$ ($T_\infty < 4.5 \text{ MK}$). This is much stronger than the constraints based on direct X-ray observations, which are approximately $T < 8.5 \text{ MK}$ ($T_\infty < 6.5 \text{ MK}$, Table 4). Additionally, the bolometric limit on the effective blackbody temperature is independent of the composition of the atmosphere of the NS. Interestingly, the dust-free limit of 3.8 MK is close to some theoretical predictions (Section 5.3.1). Given that the limit is conservative, it can be taken as an indication that the compact object is obscured by dust if it is an NS.

The constraints on the accretion rate and pulsar activity from the bolometric limits were obtained using Equations (3) and (4). The results are within a factor of 3 to those of the direct limits, as summarized in Table 5.

5.5. Implications for Other Epochs

In the above discussion, we have focused on constraints on physical properties at the times of observation. Here, we briefly

explore extrapolations of the limits to other epochs. In the case of thermal emission from an NS, the surface temperature is expected to be relatively constant from a year after explosion to current epochs (Shternin & Yakovlev 2008), which implies that the current limits apply to earlier times as well. However, if thermal relaxation has occurred, then it is possible that the surface temperature has been higher than our current limits.

Accretion and pulsar properties are expected to have evolved, which implies that the current limits need to be modified if extrapolated to other epochs. These extrapolations are uncertain and rely on models of how accretion and pulsar properties evolve over time. For accretion, the basic picture is a period of rapid fallback followed by a declining tail with a time dependence of $t^{-5/3}$. This dependence can be derived from simple arguments for marginally bound gas (Rees 1988; Evans & Kochanek 1989; Phinney 1989). This means that the limit at current epochs of around $10^{-11} \eta^{-1} M_{\odot} \text{ yr}^{-1}$ corresponds to $3 \times 10^{-9} \eta^{-1} M_{\odot} \text{ yr}^{-1}$ one year after explosion. The accretion rate was predicted to be about $10^{-4} M_{\odot} \text{ yr}^{-1}$ one year after explosion (Chevalier 1989; Houck & Chevalier 1991). The discrepancy with observations was clear a few years after explosion (e.g., Suntzeff et al. 1992), and is stronger now. A feedback is indicated, which could be the radiation pressure when the radiation can first escape from the shocked region (Houck & Chevalier 1991).

The temporal evolution of a rotating dipole in vacuum (Equation (4)) is given by

$$L = \frac{2^5 \pi^4 B^2 R^6}{3 c^3 P_0^4 (1 + t/t')^2}, \quad (5)$$

where P_0 is the birth period, t is the time since birth, and

$$\begin{aligned} t' &\equiv P/2\dot{P} \\ &= 4.1 \times 10^{14} \left(\frac{M}{M_{\odot}} \right) \left(\frac{B}{10^{12} \text{ G}} \right)^{-2} \left(\frac{P}{\text{s}} \right)^2 \left(\frac{R}{10 \text{ km}} \right)^{-4} \text{ s}, \quad (6) \end{aligned}$$

where \dot{P} is the period derivative and M , the NS mass. This models the NS as a homogeneous sphere, and assumes constant magnetic field and inclination angle. This allows us to translate the current observational limits to constraints on birth properties (Figure 8). For all but very high magnetic field strengths, the limits are essentially the same because the spin-down timescale is long. However, for magnetic field strengths above $\sim 10^{16}$ G, the current period is practically independent of the birth period.

For the rotational energy of the NS to contribute a significant fraction of the explosion energy, the rotational period has to be a few milliseconds. Figure 8 excludes all initial periods shorter than 10 ms unless the magnetic field is unusually weak or unusually strong. If the field has not evolved and the pulsar formula is applicable, the rotation of the NS is thus unlikely to have contributed a significant fraction of the explosion energy, which lends some support to the hypothesis that SN 1987A was a neutrino-powered event.

5.6. Limits on a Binary Companion

The UVOIR limits can also be used to constrain a possible surviving binary companion in SN 1987A. The evolution of the progenitor Sanduleak -69° 202 is still not fully understood and some theories involve binary interaction as an explanation for the three circumstellar rings (Blondin &

Lundqvist 1993; Morris & Podsiadlowski 2007, 2009) and the peculiar properties of SN 1987A (e.g., Menon & Heger 2017; Kochanek 2018).

In Figure 6 we show a blackbody spectrum corresponding to the temperature and radius of the Sun scaled by the distance to SN 1987A. It happens to just fit below all UVOIR limits and is constrained by the SINFONI data point at $1.7 \mu\text{m}$. Therefore, the Sun can serve as the limit for a possible main-sequence companion in SN 1987A. We note that this limit only applies if our line of sight to a companion is free of dust.

We can use the bolometric limit on the compact object of $138 L_{\odot}$ to constrain a main-sequence companion even if our line of sight is obscured by dust. The mass–luminosity (M–L) relation for companion masses $2.4 < M_c \leq 7 M_{\odot}$ is (Eker et al. 2015)

$$\left(\frac{L_c}{L_{\odot}} \right) = 1.32 \left(\frac{M_c}{M_{\odot}} \right)^{3.96}, \quad (7)$$

where L_c is the companion luminosity. By imposing that $L_c < 138 L_{\odot}$, we find that $M_c < 3.2 M_{\odot}$. We test the sensitivity of this result by comparing to limits from other M–L relations. The M–L relation $L_c/L_{\odot} = (M_c/M_{\odot})^4$ (Duric 2003, p. 20) results in a limit of $M_c < 3.4 M_{\odot}$ and $M_c < 3.2\text{--}3.7 M_{\odot}$ (depending on angular momentum and metallicity) from Figure 5.11 of Salaris & Cassisi (2005).

Morris & Podsiadlowski (2009) proposed that a $15 M_{\odot}$ primary and a $5 M_{\odot}$ companion merged to form Sanduleak -69° 202. The constraints on a binary companion show that such a companion did not survive as a $5 M_{\odot}$ main-sequence star.

5.7. Remaining Possibilities

In this section, we combine all available information and explore the remaining possibilities for the compact object, which results in much stronger conclusions. Even though the limits in individual frequency intervals are relatively weak, only a few possible options remain for the compact object in SN 1987A. This is because the direct limits are corrected for absorption, but do not consider reprocessing of the absorbed energy. This is a limitation with important consequences because some of the limits (Table 5) require more than $100 L_{\odot}$ to be absorbed and it is not obvious how such large amounts of energy can escape undetected. The bolometric limits address this limitation by including reprocessing of the emission. However, the bolometric limits only consider the cases when the UVOIR emission can escape and when the UVOIR emission is absorbed by dust. This is effectively equivalent to having a minimal 1D spherical geometry and disregarding the spatial information of the observations. We stress that the bolometric limits rely on additional assumptions and are much more model-dependent.

Below, we first describe in detail the reprocessing of the thermal emission that is expected in all models involving NSs in Section 5.7.1. This is followed by our favored explanation and reasons for rejecting additional components in Section 5.7.2.

5.7.1. Thermal Surface Emission

If the compact object is an NS, then at least thermal surface emission is expected. For a gravitational mass of $1.4 M_{\odot}$ and a

local radius of 10 km, 3.1 MK corresponds to a luminosity at infinity (redshifted, observer’s frame) of $10 L_{\odot}$ (Section 5.3.1). The choice of 10 km is conservative, as a choice of 12 km would increase the luminosity by 60% for a fixed temperature (increased emitting area and decreased gravitational redshift).

The thermal emission peaks at soft X-ray energies, which is photoabsorbed locally (on-the-spot) due to the high optical depth of the ejecta for soft X-rays (Alp et al. 2018). The X-ray emission that is absorbed by the ejecta is reprocessed into dust continuum emission, and optical and UV emission lines. The fact that the very conservative limit of $22 L_{\odot}$ (Section 4.5) is close to the expected luminosity of $10 L_{\odot}$ indicates that the compact object is dust-obscured. Regardless of whether or not there are dust clumps directly along the line of sight, it is likely that a significant amount of the X-ray input would escape as thermal dust emission at (sub-)millimeter and FIR wavelengths. If the reprocessing into dust heating occurs on-the-spot and thermal dust emission escapes directly, an NS would appear as a point source in the dust emission. To fully explore this scenario, we need to analyze observations at frequencies where the dust emission peaks; investigate the dust lifetime close to the NS; model the dust composition, geometry, and temperature; model the distribution of ^{44}Ti ; and compute the radiation propagation of UVOIR photons powered by X-ray emission from an NS. This is beyond the scope of this paper and will be the subject of future studies.

The most likely alternative scenario to on-the-spot dust heating is if the mean free path of UVOIR photons in the ejecta is comparable to the spatial extent of the ejecta. In this case, the emission would diffuse on scales comparable to the size of the ejecta and be spatially mixed with the emission powered by the decay of ^{44}Ti . This is effectively what was assumed for the dust-obscured bolometric limit of $138 L_{\odot}$ (Section 4.5) because it did not consider the spatial distribution of the escaping radiation. However, if the UVOIR photons have a long mean free path, the escaping reprocessed UVOIR emission is expected to be directly observed. This means that only a certain range of intermediate mean free paths allows an NS to be hidden in the ejecta.

Future observations that spatially resolve the dust emission will provide information about the mean free path of UVOIR photons. It is unlikely that clumps of ^{44}Ti would appear as point sources if the mean free path is long because observable overdensities require the clumps of ^{44}Ti to be well-obscured by dust. In addition, it is not clear if the intrinsic distribution of ^{44}Ti allows for overdensities that can be confused with an NS (Wongwathanarat et al. 2013, 2015).

A less likely scenario is that the input from the NS surface emission somehow escapes in the MIR where observational limits are poor, possibly as hot-dust emission (see Bouchet et al. 2004; Bouchet & Danziger 2014). This is unlikely because it requires the primary emission to be reprocessed by dust with a temperature tuned such that the emission escapes detection. Furthermore, we know that the MIR fine structure lines that are predicted to be the primary cooling channels (Jerkstrand et al. 2011) have not been observed (Lundqvist et al. 2001; Bouchet et al. 2006), implying that MIR emission cannot escape the ejecta.

5.7.2. Favored Explanation and Additional Components

All things considered, we find the most likely scenario to be that the compact object in SN 1987A is a dust-obscured

thermally emitting NS. We favor this scenario regardless of whether or not the dust absorbs the UVOIR emission locally or if the mean free path for UVOIR photons is comparable to the size of the ejecta.

The bolometric limit of $138 L_{\odot}$ leaves little room for accretion and pulsar wind activity, which would appear as additional contributions to the expected thermal surface emission of $\sim 10 L_{\odot}$ (Table 5). The effects vary depending on the spectrum. For accretion, the input is most likely in the form of soft X-rays and can be treated analogously to the thermal surface emission and simply be added to the thermal luminosity in the current framework.

Pulsar wind activity is more complicated since it could extend over the entire electromagnetic spectrum. However, the luminosity from millimeter to soft X-rays is limited by the bolometric limits and the spatial extent (Chevalier & Fransson 1992) is constrained to less than $\sim 100 \text{ km s}^{-1}$ (Section 4.5). The only realistic scenario for a PWN to contribute more than $138 L_{\odot}$ would be if the spectrum is heavily gamma-ray-dominated (e.g., Vela and Geminga, Danilenko et al. 2011; Abdo et al. 2013; Kuiper & Hermsen 2015). High-energy gamma-rays escape the ejecta and are not expected to be reprocessed into lower frequencies (Alp et al. 2018). The *Fermi*/LAT limit (Table 6) is not stringent enough to rule out this scenario.

If the compact object is a radio pulsar, it would emit narrow beams of radio emission. The total radio power is $\sim 10^{29} \text{ erg s}^{-1}$ for typical radio pulsars (Lorimer & Kramer 2012; Szary et al. 2014). Even if the ejecta are free-free thick at radio wavelengths, the energy input is insufficient to significantly contribute to the heating of the ejecta. The only realistic avenue to distinguish a thermally emitting NS from a radio pulsar is if the free-free depth is low enough and the radio beams sweep our line of sight, in which case pulsed radio emission would be detected (for recent limits, see Zhang et al. 2018).

For completeness, the compact object in SN 1987A could be a BH. However, as discussed in Section 1, most studies predict that an NS formed in the explosion.

5.8. Future Observations

Below, we review the prospects for detecting the compact object in SN 1987A with future facilities. The best constraints in the radio will come from the Square Kilometre Array (SKA, Dewdney et al. 2009; Taylor 2013). SKA-low will not be able to resolve the central ejecta from the ER, but it can perform timing observations to search for pulsed emission. Because of the side lobes of $\sim 1\%$, the sensitivity of SKA-mid is limited to $\sim 1\%$ of the ER, which will have 2 mJy spots at 0.1 arcsec resolution at 8 GHz (Zanardo et al. 2013). A point limit of $\sim 0.02 \text{ mJy}$ can therefore be expected, assuming free-free absorption to be negligible. The limit could possibly be improved by an order of magnitude, depending on the uv -coverage and the ability to self-calibrate.

As discussed in Section 5.7, the thermal surface emission from an NS could be reprocessed into a point-like source in the thermal ejecta dust emission. The dust emission peaks at $200 \mu\text{m}$ (1500 GHz) and has been observed at low spatial resolution by ALMA and *Herschel* (Indebetouw et al. 2014; Zanardo et al. 2014; Matsuura et al. 2015). Higher-resolution observations may be able to detect a region of NS-heated dust.

The *James Webb Space Telescope* (JWST, Gardner et al. 2006), The Giant Magellan Telescope (GMT, Johns et al. 2012),

and The European Extremely Large Telescope (E-ELT, Gilmozzi & Spyromilio 2007) will allow for significantly deeper searches using both imaging and spectral observations in the IR and optical. However, it remains uncertain if the compact object in SN 1987A is bright at IR or optical wavelengths. A point-like source of a few L_{\odot} is expected from reprocessing of thermal X-ray emission from an NS surface into UVOIR, if not obscured by dust clouds (Section 5.7).

The Advanced Telescope for High ENergy Astrophysics (Barcons et al. 2015, 2017; Collon et al. 2015) will be unable to spatially resolve SN 1987A and any emission from the compact object will be blended with the ER emission. In addition, Orlando et al. (2015) predicted that the X-ray emission from the ER will fade, but the central parts will become brighter, primarily driven by interaction with the reverse shock. This means that SN 1987A will become brighter in X-rays toward the center where the compact object is expected to reside. However, these difficulties will be partly counteracted by the decreasing optical depth. The optical depth in the homologous expansion phase scales as $\tau \propto t^{-2}$, where t is the time elapsed since the explosion. The optical depth at 2 keV is expected to reach 3 by 2066 ± 10 (Alp et al. 2018). The error bar accounts for asymmetries of the explosion, but excludes any uncertainty in the explosion model, variance introduced by the compact object being kicked by the explosion, and CSM structure. At higher energies, this will occur much earlier, as is relevant for a PWN.

6. Summary and Conclusions

We have placed upper limits on the compact object in SN 1987A using observations at millimeter wavelengths from ALMA; NIR from VLT; optical and UV from *HST*; and X-rays from *Chandra*. We assume that the compact object would appear as a point source in images and that it only contributes to the continuum component in observed spectra. We also place constraints on the bolometric luminosity of the compact object by investigating the total energy budget of SN 1987A. Our main conclusions are as follows:

1. The only model-independent results are the direct flux limits. They are corrected for absorption, but do not include information about the reprocessing of the absorbed emission or the geometry of the system. The most constraining limit in the millimeter range of ALMA is 0.11 mJy at 213 GHz. The deepest UVOIR limits are from the spectra taken by VLT/SINFONI in the NIR and *HST*/STIS in the optical. The allowed luminosity of the compact object in the UVOIR band is approximately $1 L_{\odot}$. The X-ray limits allow luminosities less than $\sim 10^{36}$ erg s $^{-1}$, but are very sensitive to the assumed spectrum.
2. The total energy budget of SN 1987A places a bolometric limit of $22 L_{\odot}$ on the compact object if our line of sight is free of dust, or $138 L_{\odot}$ if dust-obscured. This is based on assumptions and models of the emission reprocessing, but relies on a minimal 1D spherical model of the geometry.
3. The limits can be used to constrain the effective local (unredshifted) blackbody temperature of an NS. Only the limit of 3.8 MK from the dust-free bolometric limit is close to constraining any theoretical predictions, which typically are in the range 3–4 MK. This can be taken as a

marginal indication that the compact object is obscured by dust if it is an NS.

4. The current accretion rate is limited to less than about $10^{-11} \eta^{-1} M_{\odot} \text{ yr}^{-1}$ for the simplest model of accretion. This excludes most predictions for fallback in SN 1987A (Chevalier 1989; Houck & Chevalier 1991; Suntzeff et al. 1992) and indicates some kind of feedback (Houck & Chevalier 1991).
5. The limits constrain PWN activity to 3–830 L_{\odot} , depending on assumptions about dust and spectral shape. The luminosities can be related to the magnetic field strength and spin period by modeling the NS as a rotating dipole in vacuum. The limits constrain B to be less than $(1.8\text{--}29) \times 10^{13} P^2 \text{ G s}^{-2}$. However, because of the rapid spin-down, we cannot exclude birth magnetic field strengths higher than 10^{16} G .
6. By combining all available information about radiation reprocessing and geometry, the most likely remaining scenario is that the compact object is a dust-obscured thermally emitting NS. In this case, the thermal surface emission from the NS would be reprocessed into thermal dust emission. For realistic assumptions about the dust properties and geometry, only a small parameter space remains open for additional accretion and pulsar-wind components. We stress that this result is model-dependent. The most promising avenues for detecting reprocessed surface emission from an NS are provided by *JWST*, *GMT*, *E-ELT*, and *ALMA*.

This research was funded by the Knut & Alice Wallenberg Foundation and the Swedish Research Council. S.E.W. at UCSC was supported by the NASA Theory Program (NNX14AH34G). At Garching, support by the Deutsche Forschungsgemeinschaft through Excellence Cluster Universe (EXC 153) and Sonderforschungsbereich SFB 1258 “Neutrinos and Dark Matter in Astro- and Particle Physics,” and by the European Research Council through grant ERC-AdG No. 341157-COCO2CASA is acknowledged. The research of J.C.W. is supported in part by the Samuel T. and Fern Yanagisawa Regents Professorship. This paper makes use of the following ALMA data: ADS/JAO.ALMA#2013.1.00280. S and ADS/JAO.ALMA#2015.1.00631.S. ALMA is a partnership of ESO (representing its member states), NSF (USA) and NINS (Japan), together with NRC (Canada) and NSC and ASIAA (Taiwan) and KASI (Republic of Korea), in cooperation with the Republic of Chile. The Joint ALMA Observatory is operated by ESO, AUI/NRAO, and NAOJ. The National Radio Astronomy Observatory is a facility of the National Science Foundation operated under cooperative agreement by Associated Universities, Inc. This work is based on observations collected at the European Organisation for Astronomical Research in the Southern Hemisphere under ESO programme 294.D-5033(A). This research has made use of data obtained through the High Energy Astrophysics Science Archive Research Center Online Service, provided by the NASA/Goddard Space Flight Center. Support for Programs GO-13181, GO-13405, GO-13810, GO-14333, GO-13401, GO-14753, and GO-15256 was provided by NASA through a grant from the Space Telescope Science Institute, which is operated by the Association of Universities for Research in Astronomy, Incorporated, under NASA contract NAS5-26555.

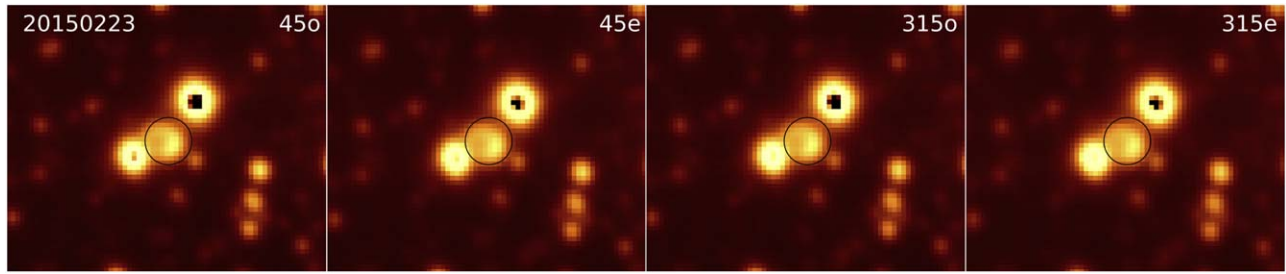


Figure 9. VLT/FORS2 circular-polarization observation of SN 1987A from 2015 February 23. The images show ordinary (o) and extraordinary (e) beams at two quarter-wave retarder plate angles of $\theta = \pm 45^\circ$. The circle centered at the position of SN 1987A ($\alpha = 83^\circ 866246$, $\delta = -69^\circ 269722$) marks an aperture of 5 pixel (1250 mas) radius within which the flux is measured. Images at other epochs show no significant variability.

STSDAS and PyRAF are products of the Space Telescope Science Institute, which is operated by AURA for NASA. The scientific results reported in this article are based to a significant degree on data obtained from the *Chandra* Data Archive. This research has made use of software provided by the *Chandra* X-ray Center (CXC) in the application package CIAO. This research has made use of NASA’s Astrophysics Data System.

Facilities: ALMA, *HST* (UVIS, STIS), VLT (FORS2, NACO, SINFONI), *CXO* (ACIS).

Software: *astropy* (Astropy Collaboration et al. 2013), *CASA* (McMullin et al. 2007), *CIAO/CALDB* (Fruscione et al. 2006), *DAOPHOT* (Stetson 1987), *DrizzlePac* (Gonzaga et al. 2012), *IRAF/PyRAF*, *matplotlib* (Hunter 2007), *MARX* (Davis et al. 2012), *numpy* (Jones et al. 2001; van der Walt et al. 2011), *scipy* (Jones et al. 2001), *STSDAS*, *Synphot* (Bushouse & Simon 1994), *XSPEC* (Arnaud 1996).

Appendix A Circular Polarimetry of SN 1987A

A.1. Observations

All observations were acquired with FORS2 mounted at the Cassegrain focus of the UT1 VLT. The observations were obtained in imaging polarimetric mode (IPOL), through the V_ HIGH FORS2 standard filter ($\lambda_0 = 555$ nm, FWHM = 123.2 nm) and with two different quarter-wave retarder plate angles of $\theta = \pm 45^\circ$ per epoch, during four epochs: 2015 February 15, 16, 18, and 23. We obtain four exposures per angle, each of 350 s. On the night of February 16, the instrument was rotated by 90° . In IPOL mode, the image is split by the Wollaston prism into two orthogonal polarized outgoing beams, ordinary (o) and extraordinary (e), and the MOS Slitlets strip mask is inserted to avoid overlapping of the beams. One of the observations is shown in Figure 9.

A.2. Methods

All frames are bias-subtracted using the corresponding calibration bias frames. A flat-field correction is not performed because of the flat-field effect (Patat & Romaniello 2006; O’Brien 2015), the additional polarization caused by the color dependent offset to the nominal retarder plate position, and the effect of the incomplete retardation of the quarter-wave plate (O’Brien 2015) gets canceled out when calculating the circular polarization using two angles. For each epoch, we group the science frames according to the quarter-wave retarder plate angle, split the ordinary and extraordinary beams, and create separate science frames, align them, and calculate the median of the four exposures. Finally, we investigate the

circular polarization of SN 1987A by performing aperture photometry with a set of different aperture radii, centered at the position of SN 1987A (Figure 9) in ordinary and extraordinary beams using the DAOPHOT.PHOT package, and calculating the circular polarization from the determined fluxes. We ignore the observations of February 18, because of variable weather conditions, which makes aperture photometry difficult. We determine the amount of circular polarization by the equation below, as described in O’Brien (2015):

$$P_V = \frac{1}{2} \left[\left(\frac{f^o - f^e}{f^o + f^e} \right)_{\theta=45^\circ} - \left(\frac{f^o - f^e}{f^o + f^e} \right)_{\theta=-45^\circ} \right], \quad (8)$$

where f^o and f^e are the measured fluxes in the ordinary and extraordinary beams, respectively. The error is calculated by propagating the photometry uncertainties.

A.3. Results

We calculated the circular polarization of SN 1987A from fluxes determined by performing aperture photometry using different aperture radii of 1, 2, 3, 4, and 5 pixels (250 mas pixel $^{-1}$), centered at the position of SN 1987A. We found that the circular polarization is consistent with zero. Figure 10 shows the circular-polarization, Stokes V values for the different aperture radii. We are unable to determine an upper limit on the circular polarization of the central ejecta because the angular resolution is insufficient for resolving the structure of SN 1987A. This leaves the circular polarization from the compact object unconstrained.

The Crab was also observed using the same setup but for a shorter duration. We are unable to detect any circular polarization in the Crab Nebula, which possibly implies that the method is relatively insensitive. A possible explanation for this is that the phase-averaged polarization is essentially zero.

Appendix B Finding Algorithm

Searches for point sources in the ejecta are made using the DAOPHOT task *daofind*. The most important input parameter for *daofind* is the local noise level (*sigma*). For ALMA images, this is set to the off-source noise in the images. We verified that this method gives essentially the same noise estimates as measurements of the noise in the visibility amplitudes. The parameter *sigma* for the UVOIR images is chosen to account for both the sky background and the Poisson noise of the ejecta. We note that both contributions are of comparable magnitude. The sky background is determined by setting a 3σ threshold such that essentially no noise peaks pass

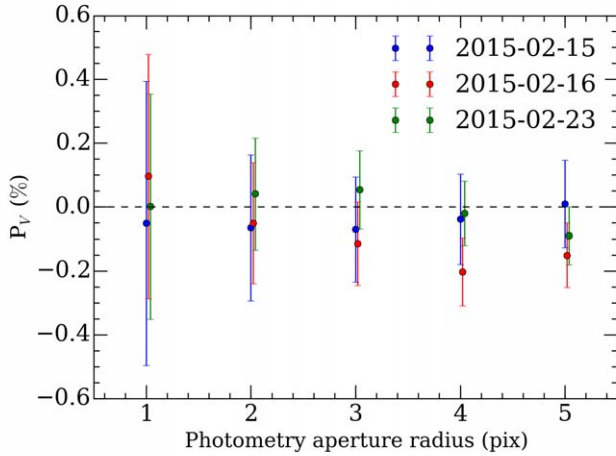


Figure 10. Circular polarization of SN 1987A measured using different aperture radii of 1, 2, 3, 4, and 5 pixels ($250 \text{ mas pixel}^{-1}$). The circular polarization is consistent with 0%.

while as many real sources as possible are detected. This transition is clearly seen as a break in the detection-threshold relation (Davis 1994). The ejecta Poisson noise is set to the square root of the maximum photon count in the original detector pixels within the search region. The parameter `sigma` is then computed as the square root of sky background and ejecta noise is added in quadrature. It is verified that the sample deviation of small segments of the central ejecta is comparable to the computed `sigma`. The effects of super-resolving when drizzling and instrument gain on the Poisson noise properties are accounted for by including a multiplicative correction factor for the geometric mapping and another factor for the gain.

Limits are determined by inserting artificial PSFs and finding the PSF flux such that it just crosses the 3σ threshold of `daofind`. The procedure is then repeated inside the search region at intervals of 12.5 mas , which is chosen to be the half-pixel size of the WFC3 and NACO images. At a few points, the detection threshold is crossed without added artificial sources, implying that point sources are detected. These are all just slightly above the detection threshold of 3σ and are interpreted as structure in the ejecta. The limits in these points are set to the maximum flux of a PSF that is consistent with the observation. None of the threshold crossing events are spatially coincident in several adjacent filters and they are not significantly increasing the upper limits.

Appendix C X-Ray Ejecta Absorption

X-ray absorption by SN ejecta is explored in detail using 3D neutrino-driven SN explosion models (Wongwathanarat et al. 2013, 2015) in an accompanying paper (Alp et al. 2018). One of the main conclusions is that the optical depth of the SN ejecta for X-rays below 10 keV is very high at the age of SN 1987A. For a discussion of the transport of the absorbed energy, see Section 4.5. Here, we use the absorption estimates based on the B15 explosion model (Woosley et al. 1988) for our X-ray analysis. The B15 model is a single-star model that was evolved to core-collapse in one dimension without mass loss. It explodes as a blue supergiant with a mass of $15.4 M_{\odot}$ and is designed to represent SN 1987A.

From the models, we compute the column number densities (N_{SN}) of H, He, C, O, Ne, Mg, Si, S, Ar, Ca, and Fe using the

Table 7
X-Ray Absorption Parameters

Element	N_{SN}^{a} (cm^{-2})	A_{SN}^{b}	$A_{\text{SN}}/A_{\text{ISM}}^{\text{c}}$
H	1.4×10^{22}	1	1
He	1.1×10^{22}	7.8×10^{-1}	8
C	1.4×10^{20}	1.0×10^{-2}	43
O	2.0×10^{20}	1.4×10^{-2}	29
Ne	4.1×10^{19}	3.0×10^{-3}	34
Mg	4.5×10^{18}	3.2×10^{-4}	13
Si	5.3×10^{19}	3.9×10^{-3}	208
S	6.6×10^{18}	4.8×10^{-4}	39
Ar	2.6×10^{18}	1.9×10^{-4}	74
Ca	1.3×10^{19}	9.4×10^{-4}	591
Fe	5.5×10^{19}	4.0×10^{-3}	148
$\text{H}_{0.1}^{\text{d}}$	1.0×10^{22}	0.73	...
$\text{H}_{0.9}^{\text{d}}$	1.8×10^{22}	1.31	...

Notes.

^a Direction-averaged SN column number density.

^b $A_{\text{SN}}(X) \equiv N_{\text{SN}}(X)/N_{\text{SN}}(\text{H})$, where X is a chemical element.

^c $A_{\text{ISM}}(X)$ is the abundance of X in the ISM from Wilms et al. (2000).

^d The quantity $\text{H}_{0.1}$ is the hydrogen column density scaled by the ratio of the direction-averaged optical depth to the 10th percentile of the optical depth at 2 keV , and $\text{H}_{0.9}$ is the 90th analogue. The column densities of other elements are assumed to be scaled by the same fraction (Alp et al. 2018).

explosion model. A single estimate cannot be made because of the asymmetries of the SN explosion. Instead, we focus on the direction-averaged column number densities and the hydrogen number densities corresponding to the 10th and 90th percentiles of the optical depth, which are shown in Table 7. The percentiles are used to represent the variance introduced by SN explosion asymmetries. Even though the hydrogen column number density $N_{\text{SN}}(\text{H})$ is relatively low, the high metallicity of the ejecta results in an optical depth of ~ 25 at 2 keV at current epochs.

Appendix D Spatial Alignment

All observations need to be accurately registered for us to use the position determined in Section 3.1, which is needed to define the search regions for the images and the extraction regions for the spectra. Only ALMA has good enough absolute astrometry. The other observations are aligned with the *HST* observations using either nearby stars or the ER, as described below.

ALMA has an absolute astrometric accuracy of less than $\sim 10 \text{ mas}$. The accuracy is determined by measuring the phase rms and using it to estimate the phase transfer error, which likely results in a quite conservative estimate. Applying a self-calibration gain table to a point source and measuring the offset, and considering the accuracy in measuring baselines both yield uncertainty estimates that are smaller than 10 mas .

Both NACO images are mapped onto the *HST*/WFC3 images using the IRAF tasks `geomap` and `geotran`. We choose 10 bright stars in the common FOV, using polynomial fitting functions, and a general geometry, which consists of shifts, scale factors, a rotation, and a skew. This aligns the images and resizes them to a common pixel size of 25^2 mas^2 . The magnification increases the pixel size from the original detector scale of 13.27^2 mas^2 , but this does not affect the

Table 8
HST Observations Used for Astrometric Registration of SN 1987A

Epoch (YYYY mm dd)	Instrument	Band	Filter	Exposure (s)	Band	Filter	Exposure (s)
2003 Jan 05	ACS	<i>R</i>	F625W	800	<i>B</i>	F435W	1200
2003 Aug 12	ACS	<i>R</i>	F625W	480	<i>B</i>	F435W	800
2003 Nov 28	ACS	<i>R</i>	F625W	800	<i>B</i>	F435W	1600
2004 Dec 15	ACS	<i>B</i>	F435W	1600
2005 Apr 02	ACS	<i>B</i>	F435W	1200
2005 Sep 26	ACS	<i>R</i>	F625W	12000
2005 Sep 28	ACS	<i>R</i>	F625W	720
2006 Apr 15	ACS	<i>R</i>	F625W	1200	<i>B</i>	F435W	1200
2006 Apr 29	ACS	<i>R</i>	F625W	720
2006 Dec 06	ACS	<i>R</i>	F625W	1200	<i>B</i>	F435W	1800
2007 May 12	WFPC2	<i>R</i>	F675W	2700	<i>B</i>	F439W	3000
2008 Feb 19	WFPC2	<i>R</i>	F675W	1600	<i>B</i>	F439W	2400
2009 Apr 29	WFPC2	<i>R</i>	F675W	1600	<i>B</i>	F439W	2000
2009 Dec 12	WFC3	<i>R</i>	F625W	3000	<i>B</i>	F438W	800
2011 Jan 05	WFC3	<i>R</i>	F625W	1000	<i>B</i>	F438W	1400
2013 Feb 06	WFC3	<i>R</i>	F625W	1200	<i>B</i>	F438W	1200
2014 Jun 15	WFC3	<i>R</i>	F625W	1200	<i>B</i>	F438W	1200
2015 May 24	WFC3	<i>R</i>	F625W	1200	<i>B</i>	F438W	1200
2016 Jun 08	WFC3	<i>R</i>	F625W	600	<i>B</i>	F438W	600

measurements because the FWHM of the point-spread function (PSF) is ~ 100 mas. Comparisons of NACO and *HST* images show that the spatial alignments are better than ~ 25 mas at the position of SN 1987A, and the rotations and skews have a negligible impact on the region relevant to this work.

The SINFONI images are aligned by fitting an elliptical band with a Gaussian radial profile to the ER. The center of the ellipse is then matched with the *HST* image position presented in Section 3.1. The accuracy is better than 20 mas, which is estimated using the diagonal elements of the covariance matrix. Alignment using nearby stars is not possible because the small FOV of SINFONI does not extend much beyond the ER. The hotspots are also poorly resolved and faint in the SINFONI images, which is why an elliptical band is used to fit the ER as an extended source.

The position of SN 1987A in the STIS observation is determined by mapping onto the *HST* images. The R.A. is determined with respect to a nearby, isolated reference star that was used for the spacecraft pointing when performing the five individual slit observations. Spectral lines from the ER are used to match the decl. with the *HST* images. This is done by fitting Gaussians to the north and south 1D profiles of the ER in the slits. The position of SN 1987A is known relative to the ER from Section 3.1. The five slits are first matched individually, allowing the sample variance to serve as an estimate of the statistical uncertainty. The average position of the five alignments is then used to align all slits. The 1σ uncertainty in the final decl. of all slits is 0.14 pixels or 7.0 mas.

The ER in the *Chandra* observation is modeled by fitting an ellipse of sinusoidal intensity along the azimuth and Gaussian radial profile (Section 3.6.1), which is also used for alignment. There are no point sources visible in the *Chandra* FOV that can be used for alignment. The error in position using this method is ~ 40 mas, which is small compared to the PSF FWHM of ~ 700 mas of *Chandra*/ACIS. The uncertainty of the position is determined by simulating samples from the model and then applying the same fitting method to resample the position.




Appendix E Observations Used for Astrometric Registration of SN 1987A

The observations that are used to determine the position of SN 1987A are listed in Table 8. The WFC3 observations are reduced as described in Section 2.4. The previous observations are described in Larsson et al. (2011).

Appendix F *Chandra* PSF

The *Chandra* PSF is created using MARX 5.3.2 (Davis et al. 2012), which is called from the CIAO task `simulate_psf`. The PSF is created for the position of SN 1987A on the CCD chip, 22 pixels off-axis (approximately the distance between the default aimpoint and optical axis), using an input spectrum extracted from the source region. The quantum efficiency of the detector is included by disabling the `ideal` option. Simulation of the readout streak and pileup are both performed. The `extended` option is disabled because the PSF is used as a convolution kernel. The PSF is simulated onto a pixel size of 50^2 mas^2 and statistical fluctuations of the simulation are reduced by making 200 iterations. The default value of 70 mas for the parameter `AspectBlur`, which is the measured uncertainty of the aspect solution, is used because it better matches the observation according to the statistical likelihood. We note that this is smaller than the “merely suggested” value of ~ 280 mas,³² which is based on a limited number of observations (Primini et al. 2011). The source of this additional blurring for at least some observations is currently not fully understood.

ORCID iDs

Dennis Alp  <https://orcid.org/0000-0002-0427-5592>
Josefin Larsson  <https://orcid.org/0000-0003-0065-2933>
Claes Fransson  <https://orcid.org/0000-0001-8532-3594>
Remy Indebetouw  <https://orcid.org/0000-0002-4663-6827>

³² <http://cxc.harvard.edu/ciao/why/aspectblur.html>

Anders Jerkstrand  <https://orcid.org/0000-0001-8005-4030>
 David Burrows  <https://orcid.org/0000-0003-0729-1632>
 Aleksandar Cikota  <https://orcid.org/0000-0001-7101-9831>
 Jacco Th. van Loon  <https://orcid.org/0000-0002-1272-3017>
 C.-Y. Ng  <https://orcid.org/0000-0002-5847-2612>
 Sangwook Park  <https://orcid.org/0000-0003-3900-7739>
 Jason Spyromilio  <https://orcid.org/0000-0001-6815-4055>
 Stan Woosley  <https://orcid.org/0000-0002-3352-7437>
 Maarten Baes  <https://orcid.org/0000-0002-3930-2757>
 Roger Chevalier  <https://orcid.org/0000-0002-9117-7244>
 Kari A. Frank  <https://orcid.org/0000-0003-0570-9951>
 B. M. Gaensler  <https://orcid.org/0000-0002-3382-3382>
 Hans-Thomas Janka  <https://orcid.org/0000-0002-0831-3330>
 Bruno Leibundgut  <https://orcid.org/0000-0002-4413-7733>
 Peter Lundqvist  <https://orcid.org/0000-0002-3664-8082>
 Mikako Matsuura  <https://orcid.org/0000-0002-5529-5593>
 Jesper Sollerman  <https://orcid.org/0000-0003-1546-6615>
 George Sonneborn  <https://orcid.org/0000-0003-1440-9897>
 Lister Staveley-Smith  <https://orcid.org/0000-0002-8057-0294>
 Giovanna Zanardo  <https://orcid.org/0000-0003-2742-771X>
 J. Craig Wheeler  <https://orcid.org/0000-0003-1349-6538>

References

- Abdo, A. A., Ajello, M., Allafort, A., et al. 2013, *ApJS*, 208, 17
 Abellán, F. J., Indebetouw, R., Marcaide, J. M., et al. 2017, *ApJL*, 842, L24
 Ackermann, M., Albert, A., Atwood, W. B., et al. 2016, *A&A*, 586, A71
 Ahmad, I., Greene, J. P., Moore, E. F., et al. 2006, *PhRvC*, 74, 065803
 Alekseev, E. N., Alekseeva, L. N., Volchenko, V. I., & Krivosheina, I. V. 1987, *JETPL*, 45, 589
 Alexeyev, E. N., Alexeyeva, L. N., Krivosheina, I. V., & Volchenko, V. I. 1988, *PhLB*, 205, 209
 Alp, D., Larsson, J., Fransson, C., et al. 2018, *ApJ*, 864, 174
 Arendt, R. G., Dwek, E., Bouchet, P., et al. 2016, *AJ*, 151, 62
 Arnaud, K. A. 1996, in ASP Conf. Ser. 101, *Astronomical Data Analysis Software and Systems V*, ed. G. H. Jacoby & J. Barnes (San Francisco, CA: ASP), 17
 Arnett, W. D., Bahcall, J. N., Kirshner, R. P., & Woosley, S. E. 1989, *ARA&A*, 27, 629
 Asaki, Y., Matsushita, S., Kawabe, R., et al. 2014, *Proc. SPIE*, 9145, 91454K
 Astropy Collaboration, Robitaille, T. P., Tollerud, E. J., et al. 2013, *A&A*, 558, A33
 Barcons, X., Barret, D., Decourchelle, A., et al. 2017, *AN*, 338, 153
 Barcons, X., Nandra, K., Barret, D., et al. 2015, *JPhCS*, 610, 012008
 Bauswein, A., Just, O., Janka, H.-T., & Stergioulas, N. 2017, *ApJL*, 850, L34
 Bevan, A. 2018, *MNRAS*, 480, 4659
 Bionta, R. M., Blewitt, G., Bratton, C. B., Casper, D., & Ciocio, A. 1987, *PhRvL*, 58, 1494
 Blondin, J. M., & Lundqvist, P. 1993, *ApJ*, 405, 337
 Blum, K., & Kushnir, D. 2016, *ApJ*, 828, 31
 Bogdanov, S. 2014, *ApJ*, 790, 94
 Boggs, S. E., Harrison, F. A., Miyasaka, H., et al. 2015, *Sci*, 348, 670
 Bonnet, H., Abuter, R., Baker, A., et al. 2004, *Msngr*, 117, 17
 Bouchet, P., & Danziger, J. 2014, in IAU Symp. 296, *Supernova Environmental Impacts*, ed. A. Ray & R. A. McCray (Cambridge: Cambridge Univ. Press), 9
 Bouchet, P., De Buizer, J. M., Suntzeff, N. B., et al. 2004, *ApJ*, 611, 394
 Bouchet, P., Dwek, E., Danziger, J., et al. 2006, *ApJ*, 650, 212
 Bratton, C. B., Casper, D., Ciocio, A., et al. 1988, *PhRvD*, 37, 3361
 Brown, G. E., Bruenn, S. W., & Wheeler, J. C. 1992, *ComAp*, 16, 153
 Brown, G. E., & Weingartner, J. C. 1994, *ApJ*, 436, 843
 Bühler, R., & Blandford, R. 2014, *RPPH*, 77, 066901
 Burrows, A. 1988, *ApJ*, 334, 891
 Burrows, D. N., Michael, E., Hwang, U., et al. 2000, *ApJL*, 543, L149
 Bushouse, H., & Simon, B. 1994, in ASP Conf. Ser. 61, *Astronomical Data Analysis Software and Systems III*, ed. D. R. Crabtree, R. J. Hanisch, & J. Barnes (San Francisco, CA: ASP), 339
 Callingham, J. R., Gaensler, B. M., Zanardo, G., et al. 2016, *MNRAS*, 462, 290
 Canizares, C. R., Davis, J. E., Dewey, D., et al. 2005, *PASP*, 117, 1144
 Cardelli, J. A., Clayton, G. C., & Mathis, J. S. 1989, *ApJ*, 345, 245
 Cash, W. 1979, *ApJ*, 228, 939
 Chatterjee, P., Hernquist, L., & Narayan, R. 2000, *ApJ*, 534, 373
 Chatterjee, S., & Cordes, J. M. 2002, *ApJ*, 575, 407
 Chatterjee, S., & Cordes, J. M. 2004, *ApJL*, 600, L51
 Chevalier, R. A. 1989, *ApJ*, 346, 847
 Chevalier, R. A., & Fransson, C. 1992, *ApJ*, 395, 540
 Chita, S. M., Langer, N., van Marle, A. J., García-Segura, G., & Heger, A. 2008, *A&A*, 488, L37
 Cohen, M., Wheaton, W. A., & Megeath, S. T. 2003, *AJ*, 126, 1090
 Collon, M. J., Vacanti, G., Günther, R., et al. 2015, *Proc. SPIE*, 9603, 96030K
 Cordes, J. M., Romani, R. W., & Lundgren, S. C. 1993, *Natur*, 362, 133
 Danilenko, A. A., Zyuzin, D. A., Shibanov, Y. A., & Zharikov, S. V. 2011, *MNRAS*, 415, 867
 Davies, R. I. 2007, *MNRAS*, 375, 1099
 Davis, J. E., Bautz, M. W., Dewey, D., et al. 2012, *Proc. SPIE*, 8443, 84431A
 Davis, L. E. 1994, *A Reference Guide to the IRAF/DAOPHOT Package* (Tucson, AZ: NOAO)
 Dewdney, P. E., Hall, P. J., Schilizzi, R. T., & Lazio, T. J. L. W. 2009, *IEEEP*, 97, 1482
 Draine, B. T. 2003, *ApJ*, 598, 1026
 Duric, N. 2003, *Advanced Astrophysics* (Cambridge: Cambridge Univ. Press)
 Dwek, E., & Arendt, R. G. 2015, *ApJ*, 810, 75
 Eisenhauer, F., Abuter, R., Bickert, K., et al. 2003, *Proc. SPIE*, 4841, 1548
 Eker, Z., Soydugan, F., Soydugan, E., et al. 2015, *AJ*, 149, 131
 Ertl, T., Janka, H.-T., Woosley, S. E., Sukhbold, T., & Ugliano, M. 2016, *ApJ*, 818, 124
 Esposito, P., Rea, N., Lazzati, D., et al. 2018, *ApJ*, 857, 58
 Evans, C. R., & Kochanek, C. S. 1989, *ApJL*, 346, L13
 Fassia, A., Meikle, W. P. S., & Spyromilio, J. 2002, *MNRAS*, 332, 296
 Faucher-Giguère, C.-A., & Kaspi, V. M. 2006, *ApJ*, 643, 332
 Fitzpatrick, E. L., & Walborn, N. R. 1990, *AJ*, 99, 1483
 France, K., McCray, R., Penton, S. V., et al. 2011, *ApJ*, 743, 186
 Frank, J., King, A., & Raine, D. J. 2002, *Accretion Power in Astrophysics* (3rd ed.; Cambridge: Cambridge Univ. Press), 398
 Frank, K. A., Zhekov, S. A., Park, S., et al. 2016, *ApJ*, 829, 40
 Fransson, C., & Kozma, C. 2002, *NewAR*, 46, 487
 Fransson, C., Larsson, J., Migotto, K., et al. 2015, *ApJL*, 806, L19
 Fransson, C., Larsson, J., Spyromilio, J., et al. 2013, *ApJ*, 768, 88
 Fransson, C., Larsson, J., Spyromilio, J., et al. 2016, *ApJL*, 821, L5
 Fruchter, A. S., & Hook, R. N. 2002, *PASP*, 114, 144
 Fruscione, A., McDowell, J. C., Allen, G. E., et al. 2006, *Proc. SPIE*, 6270, 62701V
 Fryer, C. L. 1999, *ApJ*, 522, 413
 Gaia Collaboration, Brown, A. G. A., Vallenari, A., et al. 2016a, *A&A*, 595, A2
 Gaia Collaboration, Prusti, T., de Bruijne, J. H. J., et al. 2016b, *A&A*, 595, A1
 Gardner, J. P., Mather, J. C., Clampin, M., et al. 2006, *SSRv*, 123, 485
 Garmire, G. P., Bautz, M. W., Ford, P. G., Nousek, J. A., & Ricker, G. R., Jr. 2003, *Proc. SPIE*, 4851, 28
 Gilmozzi, R., & Spyromilio, J. 2007, *Msngr*, 127, 11
 Gnedin, O. Y., Yakovlev, D. G., & Potekhin, A. Y. 2001, *MNRAS*, 324, 725
 Gonzaga, S., Hack, W., Fruchter, A., & Mack, J. 2012, *The DrizzlePac Handbook* (Baltimore: STScI operated by AURA for NASA)
 Gordon, K. D., Clayton, G. C., Misselt, K. A., Landolt, A. U., & Wolff, M. J. 2003, *ApJ*, 594, 279
 Gould, A., & Uza, O. 1998, *ApJ*, 494, 118
 Graves, G. J. M., Challis, P. M., Chevalier, R. A., et al. 2005, *ApJ*, 629, 944
 Grebenev, S. A., Lutovinov, A. A., Tsygankov, S. S., & Winkler, C. 2012, *Natur*, 490, 373
 Gröningsson, P., Fransson, C., Leibundgut, B., et al. 2008a, *A&A*, 492, 481
 Gröningsson, P., Fransson, C., Lundqvist, P., et al. 2008b, *A&A*, 479, 761
 Haberl, F., Geppert, U., Aschenbach, B., & Hasinger, G. 2006, *A&A*, 460, 811
 Hebel, K., Lattimer, J. M., Pethick, C. J., & Schwenk, A. 2013, *ApJ*, 773, 11
 Helder, E. A., Broos, P. S., Dewey, D., et al. 2013, *ApJ*, 764, 11
 H.E.S.S. Collaboration, Abramowski, A., Aharonian, F., et al. 2015, *Sci*, 347, 406
 Hirata, K., Kajita, T., Koshihara, M., Nakahata, M., & Oyama, Y. 1987, *PhRvL*, 58, 1490
 Hirata, K. S., Kajita, T., Koshihara, M., et al. 1988, *PhRvD*, 38, 448
 Ho, W. C. G., & Heinke, C. O. 2009, *Natur*, 462, 71
 Ho, W. C. G., Potekhin, A. Y., & Chabrier, G. 2008, *ApJS*, 178, 102
 Hobbs, G., Lorimer, D. R., Lyne, A. G., & Kramer, M. 2005, *MNRAS*, 360, 974
 Houck, J. C., & Chevalier, R. A. 1991, *ApJ*, 376, 234
 Hunter, J. D. 2007, *CSE*, 9, 90
 Indebetouw, R., Matsuura, M., Dwek, E., et al. 2014, *ApJL*, 782, L2
 Jerkstrand, A., Fransson, C., & Kozma, C. 2011, *A&A*, 530, A45

- Jerkstrand, A., Timmes, F. X., Magkotsios, G., et al. 2015, *ApJ*, **807**, 110
- Johns, M., McCarthy, P., Raybould, K., et al. 2012, *Proc. SPIE*, **8444**, 84441H
- Jones, E., Oliphant, T., Peterson, P., et al. 2001, SciPy: Open Source Scientific Tools for Python, <https://www.scipy.org/>
- Kallivayalil, N., van der Marel, R. P., Besla, G., Anderson, J., & Alcock, C. 2013, *ApJ*, **764**, 161
- Kirshner, R. P., Sonneborn, G., Crenshaw, D. M., & Nassiopoulos, G. E. 1987, *ApJ*, **320**, 602
- Kjær, K., Leibundgut, B., Fransson, C., et al. 2007, *A&A*, **471**, 617
- Kjær, K., Leibundgut, B., Fransson, C., Jerkstrand, A., & Spyromilio, J. 2010, *A&A*, **517**, A51
- Klochkov, D., Suleimanov, V., Pühlhofer, G., et al. 2015, *A&A*, **573**, A53
- Kochanek, C. S. 2018, *MNRAS*, **473**, 1633
- Kozma, C., & Fransson, C. 1992, *ApJ*, **390**, 602
- Kuiper, L., & Hermens, W. 2015, *MNRAS*, **449**, 3827
- Lakićević, M., van Loon, J. T., Patat, F., Staveley-Smith, L., & Zanardo, G. 2011, *A&A*, **532**, L8
- Lakićević, M., van Loon, J. T., Stanke, T., De Breuck, C., & Patat, F. 2012a, *A&A*, **541**, L1
- Lakićević, M., Zanardo, G., van Loon, J. T., et al. 2012b, *A&A*, **541**, L2
- Larsson, J., Fransson, C., Kjær, K., et al. 2013, *ApJ*, **768**, 89
- Larsson, J., Fransson, C., Östlin, G., et al. 2011, *Natur*, **474**, 484
- Larsson, J., Fransson, C., Spyromilio, J., et al. 2016, *ApJ*, **833**, 147
- Lawrence, S. S., Sugerman, B. E., Bouchet, P., et al. 2000, *ApJL*, **537**, L123
- Lenzen, R., Hartung, M., Brandner, W., et al. 2003, *Proc. SPIE*, **4841**, 944
- Lorimer, D. R., & Kramer, M. 2012, *Handbook of Pulsar Astronomy* (Cambridge, UK: Cambridge Univ. Press)
- Lucy, L. B., Danziger, I. J., Gouiffes, C., & Bouchet, P. 1989, in IAU Coll. 120: Structure and Dynamics of the Interstellar Medium, Vol. 350, ed. G. Tenorio-Tagle, M. Moles, & J. Melnick (Berlin: Springer), 164
- Lucy, L. B., Danziger, I. J., Gouiffes, C., & Bouchet, P. 1991, in *Supernovae*, ed. S. E. Woosley (New York: Springer), 82
- Lundqvist, P., Kozma, C., Sollerman, J., & Fransson, C. 2001, *A&A*, **374**, 629
- Manchester, R. N., Hobbs, G. B., Teoh, A., & Hobbs, M. 2005, *AJ*, **129**, 1993
- Matsuura, M., Dwek, E., Barlow, M. J., et al. 2015, *ApJ*, **800**, 50
- Matsuura, M., Dwek, E., Meixner, M., et al. 2011, *Sci*, **333**, 1258
- Matsuura, M., Indebetouw, R., Woosley, S., et al. 2017, *MNRAS*, **469**, 3347
- McCray, R. 1979, in *Active Galactic Nuclei*, ed. C. Hazard & S. Mitton (Cambridge: Cambridge Univ. Press), 227
- McCray, R. 1993, *ARA&A*, **31**, 175
- McCray, R., & Fransson, C. 2016, *ARA&A*, **54**, 19
- McMullin, J. P., Waters, B., Schiebel, D., Young, W., & Golap, K. 2007, in ASP Conf. Ser. 376, *Astronomical Data Analysis Software and Systems XVI*, ed. R. A. Shaw, F. Hill, & D. J. Bell (San Francisco, CA: ASP), 127
- Menon, A., & Heger, A. 2017, *MNRAS*, **469**, 4649
- Michael, E., McCray, R., Chevalier, R., et al. 2003, *ApJ*, **593**, 809
- Mitchell, R. C., Baron, E., Branch, D., et al. 2002, *ApJ*, **574**, 293
- Modigliani, A., Hummel, W., Abuter, R., et al. 2007, *arXiv:astro-ph/0701297*
- Mori, K., & Ho, W. C. G. 2007, *MNRAS*, **377**, 905
- Morris, T., & Podsiadlowski, P. 2007, *Sci*, **315**, 1103
- Morris, T., & Podsiadlowski, P. 2009, *MNRAS*, **399**, 515
- Morrison, R., & McCammon, D. 1983, *ApJ*, **270**, 119
- Ng, C.-Y., Gaensler, B. M., Murray, S. S., et al. 2009, *ApJL*, **706**, L100
- Ng, C.-Y., Gaensler, B. M., Staveley-Smith, L., et al. 2008, *ApJ*, **684**, 481
- Ng, C.-Y., Potter, T. M., Staveley-Smith, L., et al. 2011, *ApJL*, **728**, L15
- Ng, C.-Y., Zanardo, G., Potter, T. M., et al. 2013, *ApJ*, **777**, 131
- O'Brien, K. 2015, User Manual, issue 96.0, VLT-MAN-ESO-13100-1543 (European Southern Observatory)
- O'Dell, S. L., Swartz, D. A., Tice, N. W., et al. 2013, *Proc. SPIE*, **8859**, 88590F
- Orlando, S., Miceli, M., Pumo, M. L., & Bocchino, F. 2015, *ApJ*, **810**, 168
- Özel, F., & Freire, P. 2016, *ARA&A*, **54**, 401
- Page, D., Lattimer, J. M., Prakash, M., & Steiner, A. W. 2009, *ApJ*, **707**, 1131
- Panagia, N. 1999, in IAU Symp. 190, *New Views of the Magellanic Clouds*, ed. Y.-H. Chu et al. (San Francisco, CA: ASP), 549
- Panagia, N., Gilmozzi, R., Macchetto, F., Adorf, H.-M., & Kirshner, R. P. 1991, *ApJL*, **380**, L23
- Park, S., Burrows, D. N., Garmire, G. P., et al. 2002, *ApJ*, **567**, 314
- Park, S., Hughes, J. P., Slane, P. O., Mori, K., & Burrows, D. N. 2010, *ApJ*, **710**, 948
- Park, S., Zhekov, S. A., Burrows, D. N., et al. 2011, *ApJL*, **733**, L35
- Park, S., Zhekov, S. A., Burrows, D. N., Garmire, G. P., & McCray, R. 2004, *ApJ*, **610**, 275
- Patat, F., & Romaniello, M. 2006, *PASP*, **118**, 146
- Perego, A., Hempel, M., Fröhlich, C., et al. 2015, *ApJ*, **806**, 275
- Phinney, E. S. 1989, in IAU Symp. 136, *The Center of the Galaxy*, ed. M. Morris (Dordrecht: Springer), 543
- Posselt, B., Pavlov, G. G., Suleimanov, V., & Kargaltsev, O. 2013, *ApJ*, **779**, 186
- Potter, T. M., Staveley-Smith, L., Ng, C.-Y., et al. 2009, *ApJ*, **705**, 261
- Primini, F. A., Houck, J. C., Davis, J. E., et al. 2011, *ApJS*, **194**, 37
- Rees, M. J. 1988, *Natur*, **333**, 523
- Reynolds, J. E., Jauncey, D. L., Staveley-Smith, L., et al. 1995, *A&A*, **304**, 116
- Roussel, G., Lacombe, F., Puget, P., et al. 2003, *Proc. SPIE*, **4839**, 140
- Ruiz-Lapuente, P., & Spruit, H. C. 1998, *ApJ*, **500**, 360
- Salaris, M., & Cassisi, S. 2005, *Evolution of Stars and Stellar Populations* (New York: Wiley-VCH), 400
- Sanduleak, N. 1970, *CoTol*, 89
- Schreiber, J., Thatte, N., Eisenhauer, F., et al. 2004, in ASP Conf. Ser. 314, *Astronomical Data Analysis Software and Systems (ADASS) XIII*, ed. F. Ochsenbeim, M. G. Allen, & D. Egret (San Francisco, CA: ASP), 380
- Scuderi, S., Panagia, N., Gilmozzi, R., Challis, P. M., & Kirshner, R. P. 1996, *ApJ*, **465**, 956
- Serafimovich, N. I., Shibanov, Y. A., Lundqvist, P., & Sollerman, J. 2004, *A&A*, **425**, 1041
- Shapiro, S. L. 1973, *ApJ*, **180**, 531
- Shapiro, S. L., & Teukolsky, S. A. 1983, *Black Holes, White Dwarfs, and Neutron Stars: The Physics of Compact Objects* (New York: Wiley-Interscience)
- Shternin, P. S., & Yakovlev, D. G. 2008, *AsTL*, **34**, 675
- Shtykovskiy, P. E., Lutovinov, A. A., Gilfanov, M. R., & Sunyaev, R. A. 2005, *AsTL*, **31**, 258
- Skrutskie, M. F., Cutri, R. M., Stiening, R., et al. 2006, *AJ*, **131**, 1163
- Smartt, S. J., Eldridge, J. J., Crockett, R. M., & Maund, J. R. 2009, *MNRAS*, **395**, 1409
- Spitkovsky, A. 2006, *ApJL*, **648**, L51
- Steiner, A. W., Lattimer, J. M., & Brown, E. F. 2013, *ApJL*, **765**, L5
- Stetson, P. B. 1987, *PASP*, **99**, 191
- Sukhbold, T., Ertl, T., Woosley, S. E., Brown, J. M., & Janka, H.-T. 2016, *ApJ*, **821**, 38
- Suntzeff, N. B., Phillips, M. M., Elias, J. H., Walker, A. R., & Depoy, D. L. 1992, *ApJL*, **384**, L33
- Szary, A., Zhang, B., Melikidze, G. I., Gil, J., & Xu, R.-X. 2014, *ApJ*, **784**, 59
- Taylor, A. R. 2013, in IAU Symp. 291, *Neutron Stars and Pulsars: Challenges and Opportunities after 80 years*, ed. J. van Leeuwen (Cambridge: Cambridge Univ. Press), 337
- Tziamtzis, A., Lundqvist, P., Gröningsson, P., & Nasoudi-Shoar, S. 2011, *A&A*, **527**, A35
- Urobin, V. P., Wongwanarat, A., Janka, H.-T., & Müller, E. 2015, *A&A*, **581**, A40
- van der Marel, R. P., & Kallivayalil, N. 2014, *ApJ*, **781**, 121
- van der Marel, R. P., & Sahlmann, J. 2016, *ApJL*, **832**, L23
- van der Walt, S., Colbert, S. C., & Varoquaux, G. 2011, *CSE*, **13**, 22
- Walborn, N. R., Lasker, B. M., Laidler, V. G., & Chu, Y.-H. 1987, *ApJL*, **321**, L41
- Walborn, N. R., Phillips, M. M., Walker, A. R., & Elias, J. H. 1993, *PASP*, **105**, 1240
- Walker, A. R., & Suntzeff, N. B. 1990, *PASP*, **102**, 131
- Wang, L., Wheeler, J. C., Kirshner, R. P., et al. 1996, *ApJ*, **466**, 998
- Wesson, R., Barlow, M. J., Matsuura, M., & Ercolano, B. 2015, *MNRAS*, **446**, 2089
- West, R. M., Lauberts, A., Schuster, H.-E., & Jorgensen, H. E. 1987, *A&A*, **177**, L1
- White, G. L., & Malin, D. F. 1987, *Natur*, **327**, 36
- White, R. L. 1994, in *The Restoration of HST Images and Spectra—II*, ed. R. J. Hanisch & R. L. White (Baltimore, MD: STScI), 104
- Willingale, R., Aschenbach, B., Griffiths, R. G., et al. 2001, *A&A*, **365**, L212
- Willingale, R., Starling, R. L. C., Beardmore, A. P., Tanvir, N. R., & O'Brien, P. T. 2013, *MNRAS*, **431**, 394
- Wilms, J., Allen, A., & McCray, R. 2000, *ApJ*, **542**, 914
- Wongwanarat, A., Janka, H.-T., & Müller, E. 2013, *A&A*, **552**, A126
- Wongwanarat, A., Müller, E., & Janka, H.-T. 2015, *A&A*, **577**, A48
- Wooden, D. H., Rank, D. M., Bregman, J. D., et al. 1993, *ApJS*, **88**, 477
- Woosley, S. E., Pinto, P. A., & Ensmann, L. 1988, *ApJ*, **324**, 466
- Yakovlev, D. G., Ho, W. C. G., Shternin, P. S., Heinke, C. O., & Potekhin, A. Y. 2011, *MNRAS*, **411**, 1977
- Yakovlev, D. G., & Pethick, C. J. 2004, *ARA&A*, **42**, 169
- Zanardo, G., Staveley-Smith, L., Indebetouw, R., et al. 2014, *ApJ*, **796**, 82
- Zanardo, G., Staveley-Smith, L., Ng, C.-Y., et al. 2013, *ApJ*, **767**, 98
- Zhang, S.-B., Dai, S., Hobbs, G., et al. 2018, *MNRAS*, **479**, 1836